

國立交通大學

電機與控制工程研究所

碩士論文

靜電式振動電能轉換器之改良與測試

**Improvement and Testing of an Electrostatic  
Vibration-to-Electric Energy Converter**

研究生：郭炯廷

指導教授：邱一 博士

中華民國九十五年九月

靜電式振動電能轉換器之改良與測試

**Improvement and Testing of an Electrostatic  
Vibration-to-Electric Energy Converter**

研 究 生：郭炯廷

Student: Chiung-Ting Kuo

指 導 教 授：邱一

Advisor: Yi Chiu

國立交通大學 電機學院

電機與控制工程研究所

碩士論文

A Thesis

Submitted to Department of Electrical and Control Engineering  
College of Electrical and Computer Engineering

National Chiao Tung University

In Partial Fulfillment of the Requirement

For the Degree of

Master

In

Electrical and Control Engineering

September 2006

Hsinchu, Taiwan, R.O. C

中華民國九十五年九月

## 中文摘要

微機電系統 MEMS 是以半導體產業中的平面製造觀念為基礎的一種整合技術。微機電系統中的各種感測器或致動器的發展，均以和 IC 整合而形成智慧型的模組或系統作為最終目標。當微系統的技術越來越成熟時，各種利用微感測器或微傳感器所形成的智慧型網路或系統應用也隨之而生。在這些應用上，每一個標器或節點的模組都可能有微型獨立電源的需求。拜先進的超大型積體電路與 CMOS 技術所賜，現今這些微系統節點的電能需求已降至數十  $\mu\text{W}$  的程度。因此，利用微機電技術將環境中的能源轉換成電能來取代傳統的電池會是一個具有吸引力的方法。

靜電式振動電能轉換器可將生活中普遍存在的振動轉換為可用之電源，其運作原理在於，利用由振動驅動的可變電容器的改變，搭配直流電壓源產生電流輸出。轉換器的核心可變電容是利用 SOI 晶片搭配深蝕刻製程，製造梳齒狀電極而成。本實驗室先前已完成此轉換器之設計與製造，然而，系統分析及模擬並未考慮輸出端負載的效應，輸出電壓過高也造成無法與後端功率管理電路相容，而製作完成的元件因為寄生電阻電容的存在影響了轉換器特性，因此，根據先前的經驗和實驗結果，本篇論文的重點在於此轉換器之改良與測試。

系統分析及模擬平台已經修正，第二代元件的設計、製作流程及測試平台亦完成改良。根據設計，轉換器在 3.3 V 的輸入電壓下，考慮 8 M $\Omega$  的輸出負載，輸出功率能達到 200  $\mu\text{W}$  (功率密度每立方公分 105  $\mu\text{W}$ )，以及約 40 V 的輸出電壓。元件成品大小約 0.8 $\times$ 1.4 $\times$ 1.7 cm<sup>3</sup>。雖然製程良率太低導致經過機械特性測試之後，沒有元件能夠進行輸出功率量測，但透過更完整的振動測試已得到元件共振頻率與振幅。元件的電性量測也顯示，寄生電容和電阻並不存在。此外，製程條件的影響和良率過低的原因也完成討論。

## Abstract

Micro-Electro-Mechanical System (MEMS) is a technology platform based on the planar fabrication processes in the IC industry. The goal of MEMS actuators and sensors is the integration with circuits to form a smart module or system. Recent advances in the CMOS technology have reduced the power consumption of the micro system nodes to tens to hundreds of microwatts. Therefore, it is attractive to scavenge and transform the energy in the environment into electric energy.

An electrostatic vibration-to-electric energy converter can convert vibrations into electric energy. The device produces an current output from a DC voltage source. The core of the converter is a variable capacitor formed by comb fingers fabricated in a SOI wafer with DRIE processes. In our previous work, the effect of load on the output port was not considered in the device design. The output voltage was too high to be compatible to the power management circuit. Besides, parasitic conductance affected the characteristics of the fabricated device. Therefore, this thesis focuses on the improvement and testing of the electrostatic vibration-to-electric energy converter.

In this thesis, system analysis and simulation were improved for the design of the second generation device. The measurement setup and new fabrication processes were also developed. For the 3.3 V supply voltage and the optimal load of 8 M $\Omega$ , the output power was 200  $\mu$ W with the output voltage of 40 V. The fabricated device had a size of 0.8 $\times$ 1.4 $\times$ 1.7 cm<sup>3</sup>. The low yield of device fabrication caused no device with fine electrical properties to survive, and thus the output power measurement could not be conducted. However, the complete mechanical characteristics were recorded, and the unwanted parasitic conductance was eliminated. Finally, explanations for the problems in the fabrication as well as proposed solutions are discussed.

## 致謝

轉眼間，兩年的碩士生涯即將邁入尾聲，能夠完成碩士學業和論文，首先我要感謝的就是我的指導教授，邱一老師。老師對學生很用心，尤其是每個禮拜和老師一對一的個人討論，讓我深刻感受到他做研究的仔細和追求完美的執著，無形中激勵了我的做人處世態度，我覺得獲益良多。在我的論文中，老師也不厭其煩的幫我校正和修改，寫英文論文雖然辛苦，但是唸學生的論文更需要耐心和毅力，這也是我最佩服老師的地方，老師給我的感覺是亦師亦友，沒有距離，很慶幸這兩年，我選對了指導教授。

我還要感謝我的口試委員：邱俊誠教授、邵家健教授、陳科宏教授，他們對我的論文有諸多寶貴的建議和支援。當然還有學長們：林永峻、朱育杉、張文中、莊志偉，多虧了他們給我的實驗經驗和幫忙，我才能一一度過難關。

在實驗室的兩年時間，有歡笑和汗水，這一切都有實驗室成員的陪伴，均宏、建勳、忠衛、亦謙、繁果、煒智、子麟，你們讓我覺得不孤單，我很珍惜這段互相打氣、支持，以及互相帶給對方歡樂的時光，如果沒有你們的笑容，這兩年我的日子將會辛苦許多。

外系外校同學，我也要獻上深深的感激，志柏和應崇，謝謝你們對我實驗的協助，尤其是我面對不熟悉的儀器和環境時，你們的幫忙就如雪中送炭般令人感動。

蕙誼，我也謝謝你，常常需要忍受我的牢騷但是永遠都會鼓勵我。

感謝我的父母，謝謝你們永遠支持我信賴我，多虧你們的養育、供應我學費和生活費，我才能夠唸完碩士，希望我能不再讓你們操心，也希望我未來能讓你們感受到一絲驕傲。

要感謝的人真的太多，實在無法一一列舉，但是今後我都會抱著感恩的心面對週遭的每個人，謝謝！

# Table of contents

中文摘要.....	I
Abstract.....	II
致謝.....	III
Table of contents.....	i
List of figures.....	iii
List of tables.....	v
Chapter 1 Introduction.....	1
1.1 Motivation.....	1
1.2 Energy scavenging.....	1
1.2.2 Light exposure.....	2
1.2.2 Thermal gradients.....	3
1.2.3 Human power.....	4
1.2.4 Wind/air flow.....	4
1.2.5 Acoustic noise.....	4
1.2.6 Vibration.....	5
1.2.7 Summary of power sources.....	5
1.3 Vibration-to-electric energy conversion.....	6
1.3.1 Electromagnetic energy conversion.....	6
1.3.2 Piezoelectric energy conversion.....	8
1.3.3 Electrostatic energy conversion.....	9
1.3.4 Summary of vibration-to-electric conversion.....	10
1.4 Thesis objective and organization.....	10
Chapter 2 Design.....	10
2.1 Characteristics of vibration.....	12
2.2 Operation principle.....	14
2.3 Device design.....	18
2.3.1 Variable capacitor.....	18
2.3.2 Static analysis.....	21
2.3.3 Dynamic analysis.....	24
2.3.4 Spring design.....	29
2.3.5 Layout design.....	32
2.4 Circuits and energy storage.....	33
2.4.1 Measurement circuits.....	33
2.4.2 Storage device.....	35
2.5 Conclusion.....	36

Chapter 3	Fabrication process.....	37
3.1	Process flow.....	37
3.2	Discusion.....	41
3.2.1	Overheating of wafers.....	41
3.2.2	Residual stress of the oxide layer.....	46
3.3	Fabricated device.....	47
3.4	Conclusion.....	50
Chapter 4	Measurement.....	51
4.1	Mechanical measurement.....	51
4.2	Electrical measurement.....	58
4.3	Output power measurement.....	60
4.4	Conclusion.....	60
Chapter 5	Conclusion.....	62
5.1	Summary.....	62
5.2	Future work.....	63
Reference.....		66



## List of Figures

<b>Figure 1.1</b>	Thermoelectric energy converter composed of two series thermocouples..	3
<b>Figure 1.2</b>	Electromagnetic energy converter.....	7
<b>Figure 1.3</b>	Piezoelectric bimorph beam.....	8
<b>Figure 1.4</b>	(a) Gap closing and (b) overlap in-plane variable capacitor.....	9
<b>Figure 2.1</b>	Vibration spectra by Roundy.....	13
<b>Figure 2.2</b>	Vibration spectrum of an air conditioner.....	14
<b>Figure 2.3</b>	Vibration capacitor schematic.....	14
<b>Figure 2.4</b>	(a) Operation of the electrostatic energy converter and (b) Output terminal voltage $V_L$ .....	15
<b>Figure 2.5</b>	Variable capacitor at $C_{max}$ position: (a) without coating, and (b) with dielectric coating.....	17
<b>Figure 2.6</b>	Equivalent $C_{total}$ .....	17
<b>Figure 2.7</b>	Top view of the in-plane gap closing variable capacitor.....	19
<b>Figure 2.8</b>	Output power ( $\mu W$ ) for various $R_L$ and $C_{stor}$ .....	23
<b>Figure 2.9</b>	Output saturation voltage and power vs. initial finger gap ( $R_L = 8 M\Omega$ , $C_{stor} = 20 nF$ ).....	23
<b>Figure 2.10</b>	Schematic of the conversion dynamic model.....	24
<b>Figure 2.11</b>	Dynamic simulation diagram.....	26
<b>Figure 2.12</b>	Maximum displacement and spring constant for various attached mass.....	27
<b>Figure 2.13</b>	Output voltage vs. time .....	27
<b>Figure 2.14</b>	Schematic of a pair of finger gaps.....	28
<b>Figure 2.15</b>	Spring structure top view.....	30
<b>Figure 2.16</b>	Schematic of the current device.....	32
<b>Figure 2.17</b>	Schematic of the previous device.....	33
<b>Figure 2.18</b>	Measurement circuit by Roundy.....	33
<b>Figure 2.19</b>	Modified circuit schematic.....	34
<b>Figure 2.20</b>	AC output current.....	35
<b>Figure 2.21</b>	Lithium-ion rechargeable battery.....	36
<b>Figure 3.1</b>	Processing steps.....	40
<b>Figure 3.2</b>	Die and carrier wafer for DRIE.....	42
<b>Figure 3.3</b>	Sideways etched fingers: (a) illustration and (b) sideview.....	42
<b>Figure 3.4</b>	Cross section of broken fingers.....	43
<b>Figure 3.5</b>	RIE lag effect .....	43
<b>Figure 3.6</b>	Burned photoresist due to poor cooling.....	45
<b>Figure 3.7</b>	Broken structures due to residual stress.....	46
<b>Figure 3.8</b>	Overview of the device: (a) SEM photograph from frontside and (b)	



optical microscope photograph from backside.....48

**Figure 3.9** (a) Width, (b) perpendicularity of etched fingers.....49

**Figure 3.10** Overview of mass attachment.....50

**Figure 4.1** (a) Schematic and (b) photograph of the mechanical measurement setup.52

**Figure 4.2** Resonant frequency with various width of springs.....53

**Figure 4.3** Measured and simulated spring constants with feature size shrinkage considered.....53

**Figure 4.4** Fingers under (a) 0 Hz and (b) 2160 Hz vibration.....54

**Figure 4.5** Displacement of Y and Z.....55

**Figure 4.6** System response.....55

**Figure 4.7** Device resonance at 156 Hz with maximum displacement.....56

**Figure 4.8** Variable capacitor at (a)  $C_{\min}$  position and (b)  $C_{\max}$  position.....58

**Figure 5.1** Improved device fabrication: (a) pit holes etched in a Pyrex wafer, (b) anodic bond and (c) structure defined by DRIE.....62

**Figure 5.2** Principle of electret-based generator.....63



## List of tables

<b>Table 1.1</b> Comparison of energy scavenging and power sources.....	6
<b>Table 2.1</b> Design parameters of the energy converter.....	28
<b>Table 2.2</b> Spring design and safety factor.....	31



# Chapter 1 Introduction

## 1.1 Motivation

When portable microelectronic devices, such as biomedical, military, and environmental wireless micro-sensors continue to shrink and incorporate more functions, energy or power becomes insufficient. Furthermore, energy stored in the storage devices, such as batteries [1], micro-batteries [2], micro-fuel cells [3], ultra capacitors [4], micro-heat engines [5], and radioactive materials [6], is limited at small scales, resulting in short lifetime [7]. In order to lengthen the life of the portable devices, it is necessary to design the system with higher efficiency and minimize its power loss. Researchers also attempt to increase the energy density in those storage devices, but the solutions still have finite lifetime and high maintenance costs.

Advances in the low power CMOS technology along with the low duty cycles of wireless sensors have reduced power requirements to tens to hundreds of microwatts [8]. It becomes possible to power these sensor nodes by scavenging ambient energy from the environment. Therefore, it is attractive to design a self-renewable energy device that can replenish part or all of the consumed energy by utilizing the scavenged energy from the surrounding environment.

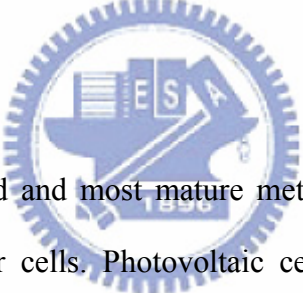
## 1.2 Energy scavenging

State-of-art scavengers and converters can extract energy from ambient natural sources, such as light exposure, thermal gradients, human power, air flow, acoustic noise, and vibration [9].

Energy scavenging means to convert ambient energy into usable electrical energy. Compared with the energy stored in common storage elements like fuel cells and batteries, the environment represents an inexhaustible energy source. As a result, energy scavenging methods introduced below are all characterized by their power density.

Various approaches to scavenge energy from the environment to power low power electronics are compared in this section. Finally, electrostatic vibration-to-electric energy conversion using the micro-electro-mechanical systems (MEMS) technology is chosen in this thesis because of its compatibility to IC processes and the characteristic of the power source.

### 1.2.1 Light exposure



The most commonly used and most mature method to scavenge energy is the photovoltaic cells or the solar cells. Photovoltaic cells convert incident light into electricity [10]. In direct sunlight at midday, photovoltaic cells offer an excellent and technically mature solution. Silicon photovoltaic cells have efficiencies ranging from 12% to 25% for single crystal silicon. Thin film polycrystalline and amorphous silicon photovoltaic cells are also commercially available. They cost less than single crystal silicon cells but have lower efficiency [11]. Overall, photovoltaic energy conversion offers high output power besides being a mature IC-compatible technology. Nevertheless, its power output depends heavily on environmental conditions and light intensities. For instance, if the target application is outdoors and needs to operate primarily during the daytime, solar cells offer adequate power density up to 15 mW/cm<sup>2</sup>. However, in normal office lighting, the same solar cell will only produce about 10 μW/cm<sup>2</sup>, which is hardly enough for most applications.

## 1.2.2 Thermal gradients

Environmental temperature variations can also serve as a power source. Thermal gradients in the environment are directly converted to electric energy through the Seebeck (thermoelectric) effect [12]. For these converters, the energy conversion is based on the electric potential difference between the cold end and hot end of a thermocouple as shown in Figure 1.1. Thermoelectric materials with large Seebeck coefficients and high electrical conductivity (low electrical resistance) can improve conversion efficiency and minimize power losses. Materials typically used for thermoelectric energy conversion include  $\text{Sb}_2\text{Te}_3$ ,  $\text{Bi}_2\text{Te}_3$ , Bi-Sb, PbTe, Si-Ge, polysilicon, BiSbTeSe compounds, and InSbTe, which are not completely compatible to the IC process [12]. Furthermore, although an output power of  $40 \mu\text{W}/\text{cm}^3$  from a  $5^\circ\text{C}$  temperature gradient has been demonstrated [13], temperature differences of this level ( $5^\circ\text{C}$ ) are not common in a micro system [14]. Without large thermal gradients, the output voltage level is low and needs to be boosted. Connecting several thermocouple elements in a series configuration can be beneficial. However, large series resistance increases ohmic power losses and thus reduce the overall power efficiency.

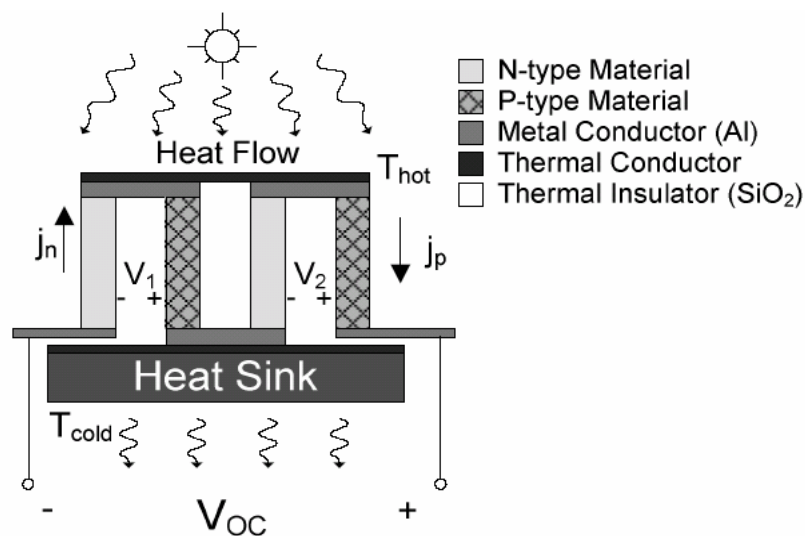


Figure 1.1 Thermoelectric energy converter composed of two series thermocouples [18]

### 1.2.3 Human power

A significant amount of work has been done on the possibility of scavenging power off the human body for use by wearable electronic devices [15,16]. The conclusion of studies undertaken at Massachusetts Institute of Technology suggested that the most energy rich and most easily exploitable source occurred at the foot during heel strike and in the bending of the ball of the foot. This research led to the development of the piezoelectric shoe inserts and the power density available from the shoe inserts was  $330 \mu\text{W}/\text{cm}^3$ . However, the problem of how to get the energy from the foot to other places on the body has not been satisfactorily solved. For an RFID tag or other wireless device worn on the shoe, the piezoelectric shoe inserts offer a good solution. Similar to temperature variation method, the application space for such devices is limited.



### 1.2.4 Wind/air flow

Wind power has been used as a power source for a long time. The potential available power from the moving air is related to the air velocity. About  $5 \text{ mW}/\text{cm}^3$  can be generated by a large windmill at a wind velocity around  $8 \text{ m/s}$  [9]. At lower air velocity, the conversion efficiency can be significantly lower and thus less power is generated (e. g.  $380 \mu\text{W}/\text{cm}^2$  at  $5 \text{ m/s}$  air velocity) [9]. However, no effort on converting air flow to electric power at very small scale (on the order of a cubic centimeter or smaller) has been reported so far.

### 1.2.5 Acoustic noise

Another source is the acoustic noise. However, there is far too little power available from acoustic noise to be of use in the scenario being investigated, except for very rare environments with extremely high noise levels [17]. Therefore, it is not a feasible power source for most applications.

### **1.2.6 Vibration**

Vibration-to-electricity conversion offers the potential for wireless sensor nodes to be self-sustaining in various environments. Most vibrations that can be utilized occur in environments such as automobiles, aircraft, ships, trains, large commercial buildings, industrial environments, and residential households. Theory and experiments show that more than  $300 \mu\text{W}/\text{cm}^3$  could be generated [9]. In this thesis, vibrations were measured on some household appliances, and the resulting spectra were used to calculate the amount of power that could be generated. A more detailed discussion of this process presented in Chapter 2 shows that conversion of vibrations to electricity can provide sufficient power for applications in certain indoor environments.

### **1.2.7 Summary of power sources**

Summary of power sources and energy storage devices is shown in Table 1.1 [9]. The top part of the table contains power sources; the bottom part of the table contains energy storage devices characterized by their energy density. Based on the survey above, vibration-to-electric energy conversion is the primary topic of the thesis due to its ubiquity and larger power density.

### 1.3 Vibration-to-electric energy conversion

Three approaches are typically used to convert vibration energy to electric energy. They are: electromagnetic (inductive), electrostatic (capacitive), and piezoelectric. In this section, these three approaches are discussed.

Table 1.1 Comparison of energy scavenging and power sources [9]

<b>Power sources</b>	<b>Power density</b> $\mu\text{W}/\text{cm}^3$ or $\mu\text{W}/\text{cm}^2$	<b>Commercially available?</b>
Solar (outdoors)	15, 000 $\mu\text{W}/\text{cm}^2$	Yes
Solar (indoors)	10 $\mu\text{W}/\text{cm}^2$	Yes
Temperature gradient	40 $\mu\text{W}/\text{cm}^3$ at 5°C gradient	Soon
Human power	330 $\mu\text{W}/\text{cm}^3$	No
Air flow	380 $\mu\text{W}/\text{cm}^3$ at 5 m/s velocity	No
Acoustic noise	0.96 $\mu\text{W}/\text{cm}^2$ at 100 dB	No
Vibration	375 $\mu\text{W}/\text{cm}^3$	No
<b>Storage devices</b>	<b>Energy density</b> $\mu\text{Wyear}/\text{cm}^3$	<b>Commercially available?</b>
Batteries (Lithium)	90	Yes
Batteries (Lithium-ion)	34	Yes
Fuel cells	110	No
Ultracapacitors	1.6~3.2	Yes
Heat engine	105	No
Radioactive ( $^{63}\text{Ni}$ )	52	No

#### 1.3.1 Electromagnetic energy conversion

Electromagnetic energy conversion uses a magnetic field to convert mechanical energy to electricity based on Faraday’s law, which states that a voltage is produced as the magnetic flux linkage changes. In such a device, a coil is attached to the oscillating mass and moves through a magnetic field established by a permanent magnet as shown in Figure 1.2 [18,19]. The produced voltage by the electromagnetic



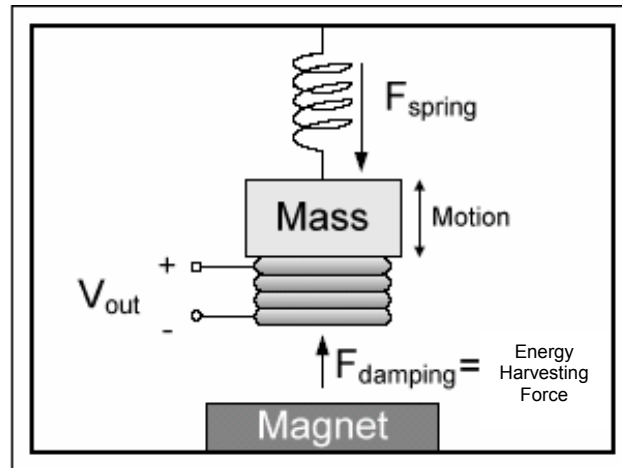


Figure 1.2 Electromagnetic energy converter [18]

converter is proportional to the magnetic field and the number of turns of the coil.

Shearwood and Yates [20] develop a device capable of producing  $0.3 \mu\text{W}$  (power density of  $10\sim 15 \mu\text{W}/\text{cm}^3$ ) from a vibration source with displacement magnitude 500 nm at 4.4 kHz. The calculated AC output voltage of the  $0.3 \mu\text{W}$  generator was 8 mV, which was too small to be rectified by a bridge rectifier that required a turn-on voltage of about 0.5 V.

More recently, Chandrakasa et al. have developed electromagnetic converters for vibrations with magnitude of about 2 cm at about 2 Hz generated by a walking person [21-23]. Their simulations showed a maximum output power of  $400 \mu\text{W}$  could be achieved with the output voltage of 180 mV. The device size was  $4 \text{ cm} \times 4 \text{ cm} \times 10 \text{ cm}$ , and therefore the corresponding power density would be  $2.5 \mu\text{W}/\text{cm}^3$ .

The most common issue is that the induced voltage of the electromagnetic converters is inherently small. Methods to increase the induced voltage include using a transformer, increasing the number of the turns of the coil, and increasing the permanent magnetic field. However, all options are limited by the available space. Another issue is that it is difficult to fabricate large number of high quality coils with planer thin film processes. Thus the power density of electromagnet converter is

lower than other types of devices.

### **1.3.2 Piezoelectric energy conversion**

Piezoelectric energy conversion converts mechanical energy to electricity by straining a piezoelectric material [9,14]. Strain in a piezoelectric material separates charge across the device and produce a voltage drop proportional to the applied stress. Typically, the oscillating system is a cantilever beam with a mass attached at the free end (Figure 1.3). When vibrations drive the device, the converter provides an AC voltage. However, in order to rectify and convert the extracted power to a stable supply, additional circuitry is needed.

Optimal power circuitry for piezoelectric generators driven by vibrations has been studied [25,26]. The maximum power output reported was 18 mW with a corresponding power density of 1.86 mW/cm<sup>3</sup>. The frequency of the driving vibrations was reported as 53.8 Hz. Prototypes of piezoelectric converters were also designed by another group [9,14,24]. The piezoelectric converter generated a power density of 200 μW/cm<sup>3</sup> for the vibration input 2.25m/s<sup>2</sup> at 120 Hz.

In the piezoelectric converter, high-piezoelectric-constant materials such as PZT are difficult to deposit and incompatible to the IC process. Most researches so far still utilize bulk materials, which is not suitable for the integrated microsystems.

### **1.3.3 Electrostatic energy conversion**

The main part of an electrostatic converter is a initially charged variable capacitor formed by a comb structure (Figure 1.4). When the movable plate moves because of vibrations, mechanical energy is transformed into electricity.

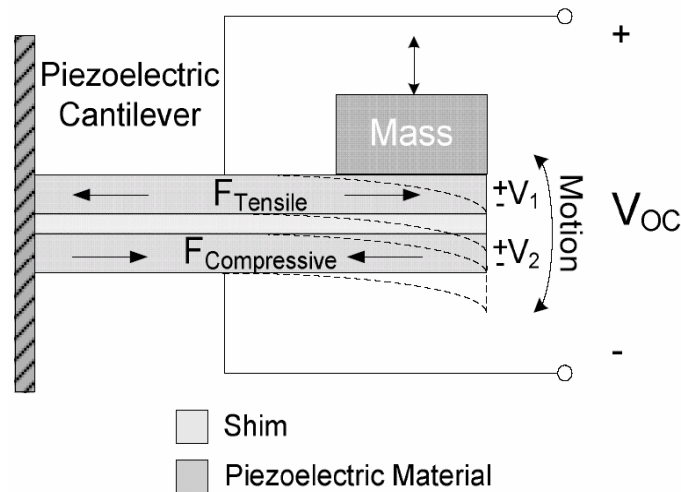


Figure 1.3 Piezoelectric bimorph beam

Meninger et al. [23] designed an electrostatic converter using MEMS technology with a silicon on insulator (SOI) wafer. Simulation shows a power output of  $8.6 \mu\text{W}$  for a device size of  $1.5 \text{ cm} \times 0.5 \text{ cm} \times 1 \text{ mm}$  from a vibration source at  $2.52 \text{ kHz}$ . They did not present any actual test results. Another design was proposed by Roundy [14] with an output power density of  $110 \mu\text{W}/\text{cm}^3$  (output voltage of  $33 \text{ V}$ ) under vibration input  $2.25 \text{ m/s}^2$  at  $120 \text{ Hz}$ .

The most attractive feature of an electrostatic energy converter is its IC process compatibility. Typically, MEMS variable capacitors are fabricated through mature silicon micromachining process, such as deep reactive ion etching (DRIE). Therefore, it is suitable to power a microsystem or sensor nodes. The electrostatic energy converter also provides high output voltage levels and moderate power density. The drawback of the converter is that it needs an external voltage source  $V_{in}$  to initially charge the variable capacitor. However, it is expected that besides powering the load, the output power can be fed back to the external voltage source and recharge it. If the output power from the energy converter exceeds the need of load terminals, the external supply voltage source has no energy loss, and the system becomes self-sustained.

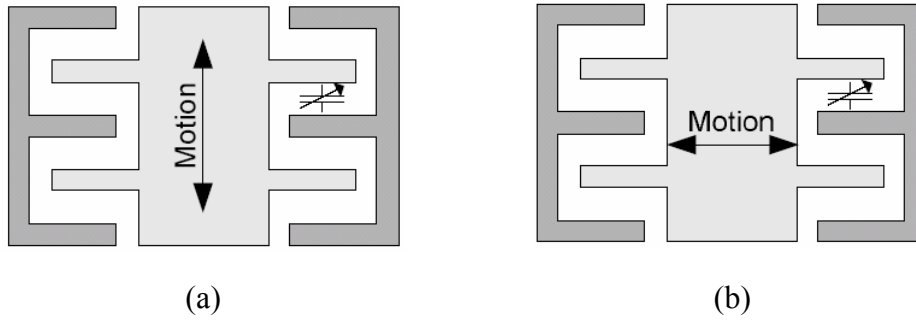


Figure 1.4 (a) Gap closing and (b) overlap in-plane variable capacitors [18]

### 1.3.4 Summary of vibration-to-electric energy conversion

According to the above literatures review, the electrostatic vibration-to-electric energy converter is studied in this thesis due to its compatibility to IC processes and the characteristic of the power source.



### 1.4 Thesis objective and organization

In our previous work [27], the system analysis and simulation of an electrostatic energy converter were accomplished. However, the effect of a resistive load on the output port was not considered. Besides, parasitic conductance led to the failure of the output power measurement. Therefore, the objectives of this thesis includes

- (a) constructing a more detail conversion model with a resistive load taken into consideration;
- (b) design a new electrostatic vibration-to-electric energy converter with higher output power and eliminate its parasitic conductance;
- (c) fabricating the device based on optimal design form the simulation;
- (d) measuring the mechanical and electrical characteristics.

In order to design the vibration to electric energy converter, the nature of

vibrations from potential sources must first be studied. Chapter 2 presents the characterization of several common occurring low level vibrations. A general conversion model and complete converter design are also presented in Chapter 2. The fabrication process, process issues and process results are described in Chapter 3. The measurement results and discussions are presented in Chapter 4. Future works is discussed in Chapter 5.



## Chapter 2 Design

Electrostatic vibration-to-electricity conversion depends on the change of capacitance of a variable capacitor caused by vibration. The variable capacitor is initially charged, and as its movable electrode oscillates because of vibration, mechanical energy is converted into electrostatic energy. After the conversion process, the converted energy is then recurrently delivered to the output port, resulting in the output current through the load.

At first, characteristics of common low-level vibration is introduced in this chapter. The operation and device design, including static and dynamic analysis, are then discussed. Finally, circuitry including energy storage devices for this converter is presented.



### 2.1 Characteristics of vibration

The output power of a vibration driven converter depends on the nature of the vibration source, which must be known in order to estimate the generated power. There are various kinds of vibrations in the environment; however, it is desired to target those most common ones in homes, office buildings, cars, and factories to maximize the potential applicability of the device. In order to estimate how much power can be converted from vibration, the details of vibration characteristics must be considered.

Measurement of various vibration sources was conducted by Roundy [9], as shown in Figure 2.1. From the spectra of these measured low-level vibrations, two conclusions can be drawn. First, the assumption of steady vibration concentrated at

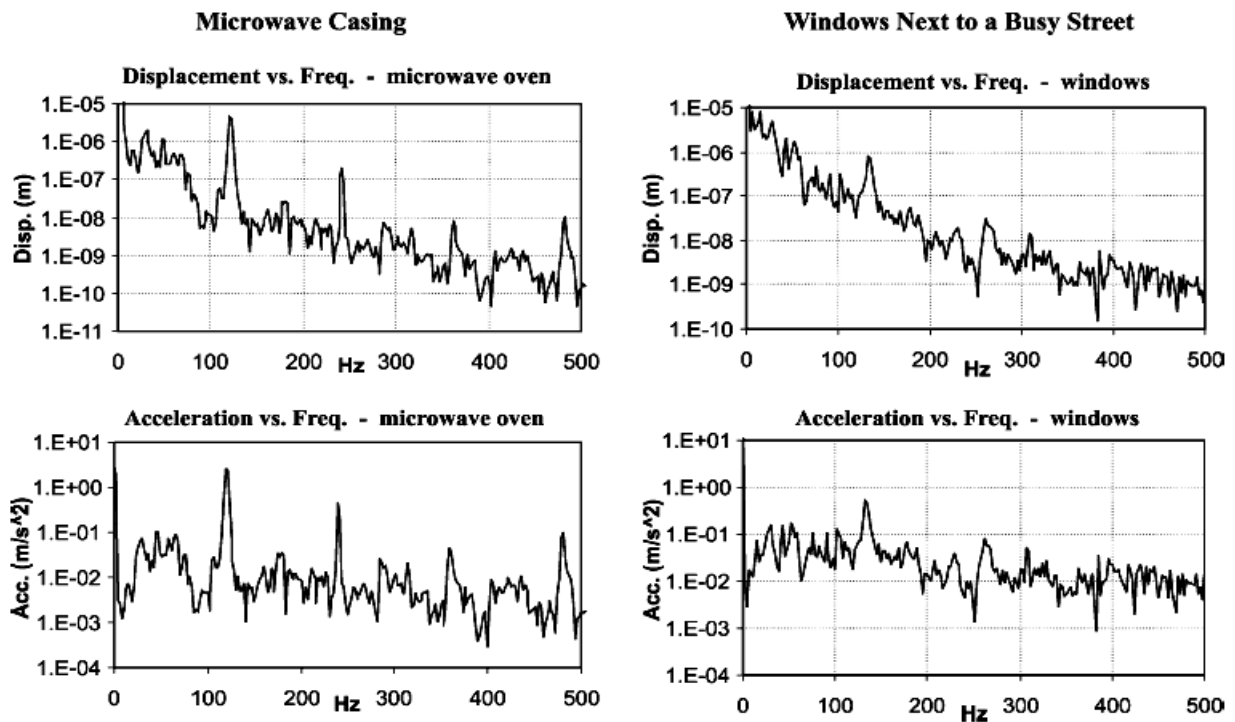


Figure 2.1 Vibration spectra by Roundy [11]

specific frequencies seems reasonable. Second, the high frequency vibration modes are lower in acceleration magnitude than the low frequency fundamental mode.

We have also measured the vibration spectrum of an air conditioner. As shown in Figure 2.2, The most energetic mode is the low-frequency one at about 120 Hz, as observed by Roundy. From Figure 2.2, it is noticed that the vibration of the air conditioner has a peak acceleration of about  $2.25 \text{ m/s}^2$  at about 120 Hz. These values are used in the following static and dynamic analysis of the energy converter to find out the optimal device design.

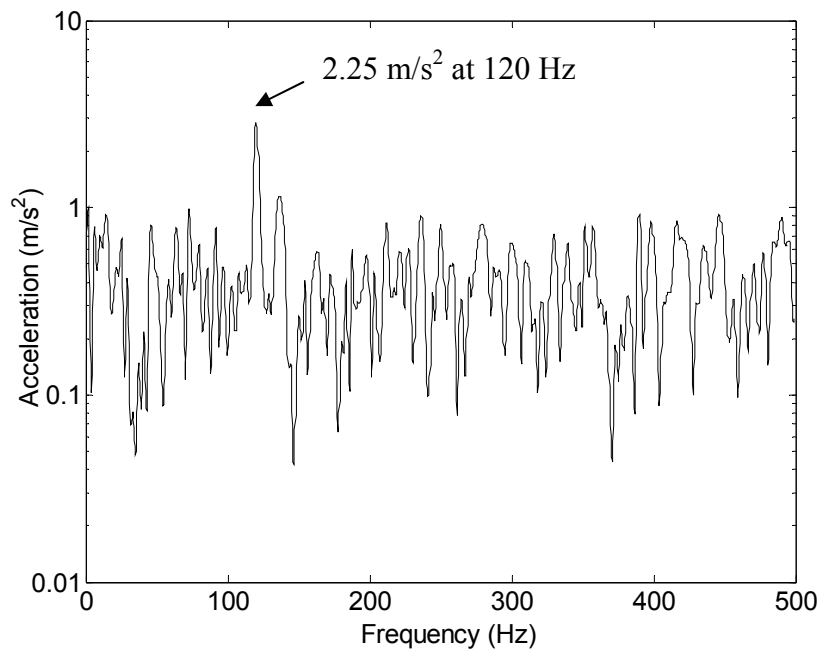


Figure 2.2 Vibration spectrum of an air conditioner

## 2.2 Operation principle

A variable capacitor  $C_v$  is the main component in the energy converter [19,30], as shown in Figure 2.3. The energy stored in the capacitor is increased when the capacitance is changed from  $C_{\max}$  to  $C_{\min}$  by to the external vibration.

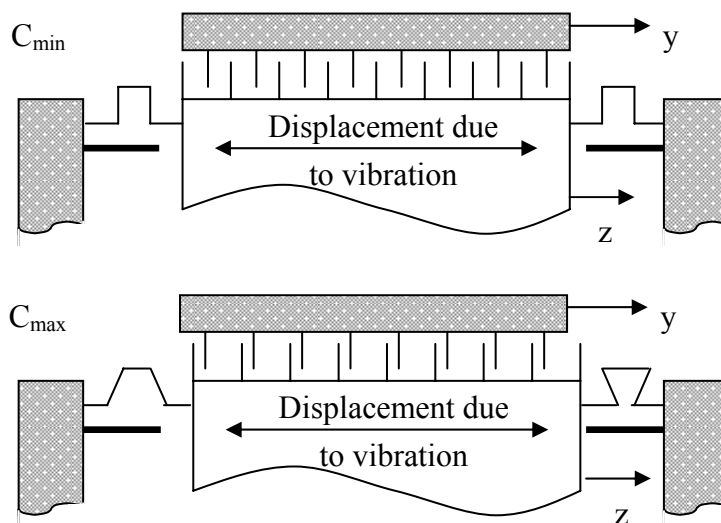


Figure 2.3 Variable capacitor schematic



Figure 2.4 (a) shows a schematic circuit that can be used to extract the converted energy. The variable capacitor  $C_v$  is charged by an external voltage source  $V_{in}$  through the switch SW1 when  $C_v$  is at its maximum  $C_{max}$ . When  $C_v$  is charged to  $V_{in}$ , SW1 is opened and then the capacitance is changed from  $C_{max}$  to  $C_{min}$  due to the electrode displacement caused by vibration. In this process, the charge  $Q$  on the capacitor remains constant (SW1 and SW2 both open). Therefore, the terminal voltage across the capacitor is increased and the vibration energy is converted to the electrostatic energy stored in the capacitor. When the capacitance reaches  $C_{min}$  ( $V_{max}$ ), SW2 is closed and the charge is transferred to a storage capacitor  $C_{stor}$ . Let the conversion cycle be  $\Delta t$ , the voltage variation of the  $n$ -th cycle before and after the charge transfer can be related by

$$V_L[n, t=t_n] = \frac{V_L[n-1, t=t_{n-1} + \Delta t] C_{stor} + V_{max} C_{min}}{C_{stor} + C_{min}}, \quad (2.1)$$

where  $V_{max}$  is equal to  $V_{in} C_{max} / C_{min}$ ,  $V_L[n, t=t_n]$  is the voltage after the charge transfer,  $V_L[n-1, t=t_{n-1} + \Delta t]$  is the voltage before the charge transfer, and  $t_n = t_{n-1} + \Delta t$ , as shown in Figure 2.4 (b).

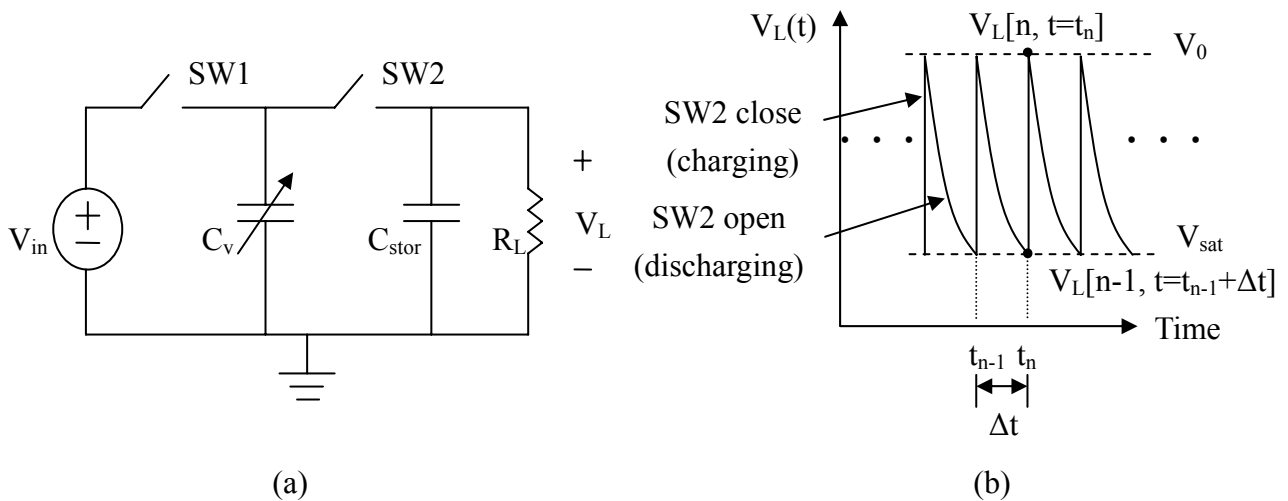


Figure 2.4 (a) Operation of the electrostatic energy converter and (b) output terminal voltage  $V_L$

SW2 is then opened and  $C_v$  varies back to  $C_{\max}$ , completing one conversion cycle. During this period  $\Delta t$ , the charge on  $C_{\text{stor}}$  is discharged by the load resistance  $R_L$  with time constant  $\tau = C_{\text{stor}}R_L$  before it is charged again by  $C_v$ . Therefore, the voltage across  $C_{\text{stor}}$  can be expressed as

$$V_L[n, t=t_n + \Delta t] = \frac{V_L[n-1, t=t_n + \Delta t]C_{\text{stor}} + V_{\max}C_{\min}}{C_{\text{stor}} + C_{\min}} \times \exp(-\Delta t/R_L C_{\text{stor}}). \quad (2.2)$$

If the charge transferred to  $C_{\text{stor}}$  is more than that discharged through the load, the net increment will result in the rises of  $V_L$  step by step. In the steady state, the net increment of charge on  $C_{\text{stor}}$  becomes zero. As shown in Figure 2.4(b), the initial and final terminal voltages  $V_L$  of the discharge process become constant,  $V_L[n, t=t_n + \Delta t] = V_L[n-1, t=t_{n-1} + \Delta t] = V_{\text{sat}}$ , Equation 2.2 is reduced to:

$$V_{\text{sat}} = \frac{V_{\text{sat}}C_{\text{stor}} + V_{\max}C_{\min}}{C_{\text{stor}} + C_{\min}} \times \exp(-\Delta t/R_L C_{\text{stor}}) \quad (2.3)$$

From Equation 2.3, that the steady-state final terminal voltage  $V_{\text{sat}}$  in the charge-discharge cycle can be expressed as

$$V_{\text{sat}} = \frac{\frac{C_{\max}V_{\text{in}}}{C_{\text{stor}}}}{(1 + \frac{C_{\min}}{C_{\text{stor}}}) \times \exp(\Delta t/R_L C_{\text{stor}}) - 1}, \quad (2.4)$$

where  $\Delta t =$  conversion cycle time  $= 1/2f$  and  $f$  is the vibration frequency. When the voltage ripple of the charge-discharge process is small, as will be shown subsequently, the output power can be estimated by,

$$P_{\text{out}} = \frac{V_{\text{sat}}^2}{R_L}. \quad (2.5)$$

For a more accurate calculation, integration of output terminal voltage is used to calculate the average power output as shown below,

$$P(t) = \frac{V_L^2(t)}{R_L} = \frac{(V_0 e^{-t/R_L C_{\text{stor}}})^2}{R_L}, \quad (2.6)$$

$$P_{\text{out}} = \frac{1}{\Delta t} \int_0^{\Delta t} P(t) dt = \frac{C_{\text{stor}} V_0^2}{2\Delta t} [1 - \exp(-2\Delta t / R_L C_{\text{stor}})], \quad (2.7)$$

where  $V_0 = V_{\text{sat}} \times e^{\Delta t / R_L C_{\text{stor}}} \propto C_{\text{max}}$  is the voltage across  $C_{\text{stor}}$  before discharging in the steady state (Figure 2.4 (b)). It can be observed that the output power is in general proportional to  $C_{\text{max}}^2$ . In the comb structure,  $C_{\text{max}}$  is determined by the minimum finger spacing. In a previous design [27], the minimum finger spacing is kept at  $0.5 \mu\text{m}$  to prevent shortage of the uninsulated fingers (Figure 2.5(a)). If a dielectric coating can be applied to the side walls of the fingers for insulation (Figure 2.5(b)), the minimum spacing can be further reduced to increase  $C_{\text{max}}$  and  $P_{\text{out}}$ . In this design, the total capacitance becomes  $C_{\text{dielectric}} \parallel C_{\text{air}} \parallel C_{\text{dielectric}}$  (Figure 2.6). Silicon nitride can be used as the dielectric material due to its process compatibility and high dielectric constant ( $\epsilon_r = 7$ ). With a  $500\text{-\AA}$ -thick nitride coating,  $C_{\text{max}}$  can be increased by a factor of four, compared to previous design. It should be noted that the dielectric coating barely increases  $C_{\text{min}}$ . Therefore, the expected increase of output power will not be affected by the change of  $C_{\text{min}}$ .

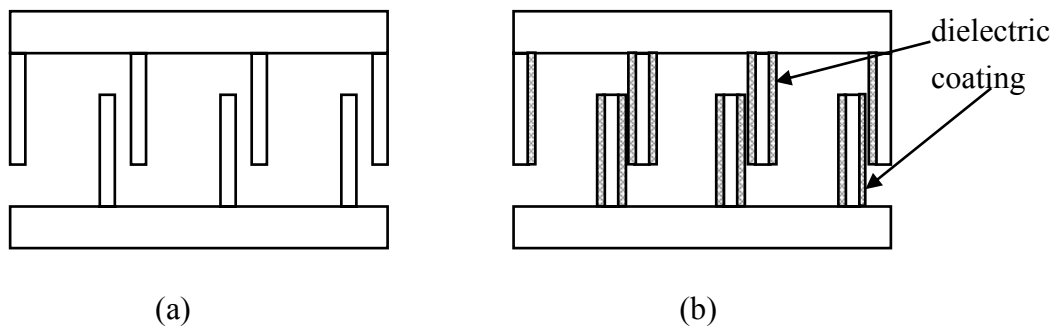


Figure 2.5 Variable capacitor at  $C_{\text{max}}$  position: (a) without coating, and (b) with dielectric coating

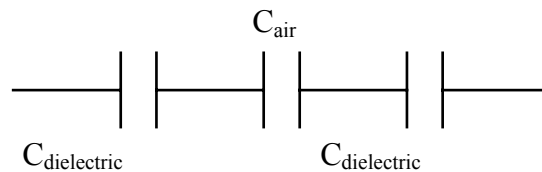


Figure 2.6 Equivalent  $C_{\text{total}}$

## 2.3 Device design

To design the device, first the topology of the variable capacitor must be explored. Based on the previous study [27], the in-plane gap closing capacitor is chosen due to the large capacitance change and system stability. The static analysis of output power using Equation 2.4 and Equation 2.5 with dielectric coating taken into consideration is then performed. Numerical Simulink simulation are used for dynamic analysis to obtain the optimal design parameters.

From Equation 2.4, the output power strongly depends on  $C_{\max}$ . Thus the main approach to increase output power is to maximize the value of the variable capacitance. Furthermore, it is desirable to target a fabrication process that can produce devices with large capacitances. A very thick device layer and a high aspect ratio are therefore necessary. This study takes advantage of the silicone-on-insulator (SOI) wafer in that it offers very thick structures (up to 200  $\mu\text{m}$  or more ). As for high aspect ratio, the deep reactive ion etching (DRIE) process is used to fabricate the devices with aspect ratio up to 20:1.

### 2.3.1 Variable capacitor

The in-plane gap closing type variable capacitor is shown in Figure 2.7. The dark areas are structures anchored to the substrate, whereas the light areas are released structures that are free to move.

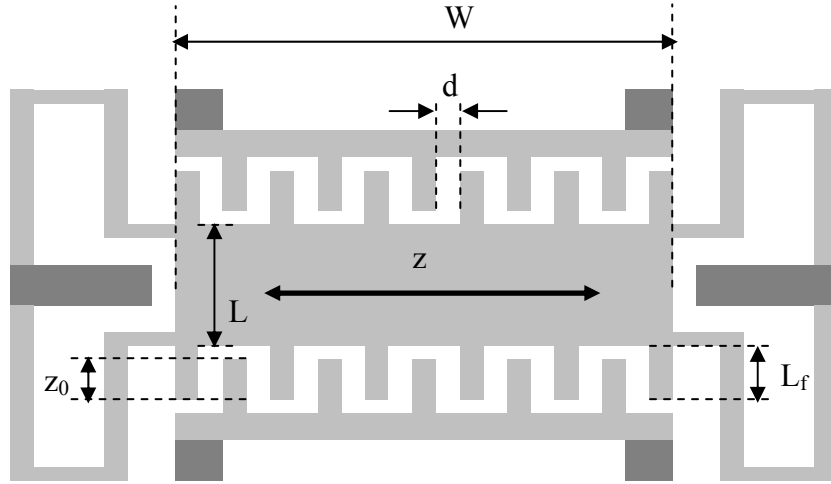


Figure 2.7 Top view of the in-plane gap closing variable capacitor

The symbols used in the following analysis are listed below.

- A : top-view area of the movable plate,
- d : initial gap between interdigitated fingers,
- $d_0$  : initial gap between the top plate and the substrate,
- $L_f$  : length of comb fingers,
- h : thickness of comb fingers,
- $N_g$  : number of gaps in the interdigitated comb fingers,
- z : displacement of the movable plate,
- $z_0$  : initial overlap length of interdigitated comb fingers,
- W : width of the plate,
- L : length of the plate.

As shown in Figure 2.7, the spring of the in-plane gap closing variable capacitor makes it easier to move perpendicular to the finger gaps. The motion is in the plane of the wafer and mechanical stops can be incorporated with standard fabrication processes. Therefore, the minimum dielectric gap and thus the maximum capacitance can be precisely controlled. The capacitance  $C_v$  without dielectric coating is

$$C_v(z) = N_g \epsilon_0 L_f h \left( \frac{2d}{d^2 - z^2} \right), \quad (2.8)$$

where  $\epsilon_0$  is the permittivity of free space. The mechanical damping including the squeeze film damping force between interdigitated fingers and the lateral air drag force between the movable plate and substrate is given by [28, 29]

$$b_m(z)\dot{z} = \left( \frac{\mu A}{d_0} + \alpha \frac{\mu N_g L_f h^3}{d^3} \frac{1}{(1-\epsilon^2)^{1.5}} \right) \dot{z}, \quad (2.9)$$

where  $\alpha \approx 1.74$  is a coefficient related to the ratio of width and length of the movable plate,  $\mu = 1.82 \times 10^{-5}$  Pa-sec is the viscosity of air at 1 atm, and  $\epsilon = \frac{z}{d}$  is the normalized displacement of the movable plate. Finally, the electrostatic force is given by

$$b_e z = \frac{-Q^2 z}{2N_g d \epsilon_0 L_f h}, \quad (2.10)$$

where  $Q$  is the charge on the variable capacitor and the minus sign indicates an attraction force.

With dielectric coating of thickness  $t$  and the removal of the substrate beneath the movable plate by backside etching process (as will be explained in Chapter 3), Equation 2.8~2.10 should be corrected as:

$$C_v(z) = N_g \epsilon_0 L_f h \left( \frac{2\left(\frac{2t}{\epsilon_r} + d - 2t\right)}{\left(\frac{2t}{\epsilon_r} + d - 2t\right)^2 - z^2} \right), \quad (2.11)$$

$$b_m(z) = \left( \alpha \frac{\mu N_g L_f h^3}{(d-2t)^3 \left[ 1 - \left( \frac{z}{d-2t} \right)^2 \right]^{1.5}} \right), \quad (2.12)$$

and

$$b_e z = \frac{-Q^2}{2N_g \epsilon_0 L_f h \left( \frac{2t}{\epsilon_r} + d - 2t \right)} z. \quad (2.13)$$

When the substrate beneath the movable plate is removed, only the squeeze film

damping force between interdigitated fingers contributes to the mechanical damping force  $b_m(z) \times \dot{z}$  (Equation 2.12). Besides, according to Equation 2.13, the electrostatic force  $b_e \times z$  is proportional to the negative displacement of the movable plate. Therefore, it acts more like a negative spring than a damper. In order to get enough change in the variable capacitance, the thickness  $h$  should be large and the displacement  $z$  should be close to the initial gap  $d$ . In our calculation, the variable capacitance can range from 44 pF to 6660 pF.

### 2.3.2 Static analysis

In Equation 2.4,  $R_L$  and  $C_{stor}$  can be chosen so that the discharging time constant  $\tau = C_{stor}R_L$  is much larger than the conversion cycle time  $\Delta t$ . The output voltage ripple in the steady state can therefore be neglected. In this case,  $V_{sat}$  can be approximated as

$$V_{sat} \approx \frac{C_{max} V_{in}}{C_{min} \left( 1 + \frac{\Delta t}{R_L C_{min}} + \frac{\Delta t}{R_L C_{stor}} \right)}, \quad (2.14)$$

Usually  $C_{min}$  is a small value (in the order of 100 pF). The other circuit components in Equation 2.14 can be chosen so that  $C_{stor} \gg C_{min}$  and  $R_L C_{min} \ll \Delta t$  and Equation 2.14 can be simplified as

$$V_{sat} \approx \frac{C_{max} V_{in}}{C_{min} \frac{\Delta t}{R_L C_{min}}} = \frac{C_{max} V_{in}}{\Delta t} R_L, \quad (2.15)$$

The power output becomes

$$P_{out} \approx \frac{V_{sat}^2}{R_L} \approx \left( \frac{C_{max} V_{in}}{\Delta t} \right)^2 R_L, \quad (2.16)$$

For a typical low-power sensor node or module, the minimum output power requirement is about 200  $\mu$ W. In addition, a power management circuit is needed to

convert the high output voltage to lower ones for various sensor and signal processing units. To be compatible with the power management circuit, the maximum output voltage should be limited to about 40 V. Inserting these constraints into Equation 2.5, one can obtain the range of  $R_L$ :

$$R_L \leq 8 \text{ M}\Omega. \quad (2.17)$$

Even though a smaller  $R_L$  can be used, this would require increasing  $C_{\max}$  in order to satisfy the voltage and power requirement (Equation 2.15 and Equation 2.16), which in turn will have adverse effects in the dynamic behavior of the converter. Therefore,  $R_L = 8 \text{ M}\Omega$  and hence the calculated  $C_{\max}$  of about 6.7 nF are used in the following calculation.

Based on Equation 2.4 and Equation 2.5, the output power  $P_{\text{out}}$  for various  $C_{\text{stor}}$  and  $R_L$  is shown in Figure 2.8. For  $C_{\text{stor}} \gg C_{\text{min}}$  (44 pF), it can be seen that the output power does not depend on the storage capacitor  $C_{\text{stor}}$  when it is relatively large. Nevertheless, a large  $C_{\text{stor}}$  will result in long initial charge time when the converter starts to work from a static status. Hence, a reasonable  $C_{\text{stor}}$  of 20 nF is used.

From Equation 2.4 and with the values of  $C_{\text{stor}}$  and  $R_L$  obtained from above, input voltage  $V_{\text{in}}$  of 3.3 V, vibration frequency of 120 Hz, and chip area size of  $1 \text{ cm}^2$ , Figure 2.9 shows the calculated output saturation voltage and power as a function of the initial finger gap distance and the thickness of the silicon nitride layer. The finger thickness, length, and width are 200  $\mu\text{m}$ , 1200  $\mu\text{m}$  and 10  $\mu\text{m}$ , respectively [27]. The dimension of the fingers are based on the available deep etching process capability. The minimum gap distance is assumed to be 0.1  $\mu\text{m}$ , which is controlled by mechanical stops. It can be seen that with a 500-Å-thick nitride, the initial finger gap has an optimal value of 35  $\mu\text{m}$  for a power output of 200  $\mu\text{W}$  and output voltage of 40 V. Although a smaller initial finger gap can be also designed to generate enough power, the increased electrostatic force between interdigitated fingers (which causes



larger proof mass needed to initiate the vibration of the device) is not desirable in the dynamics of the microstructure. Therefore, only the optimal value of 35  $\mu\text{m}$  is preferred.

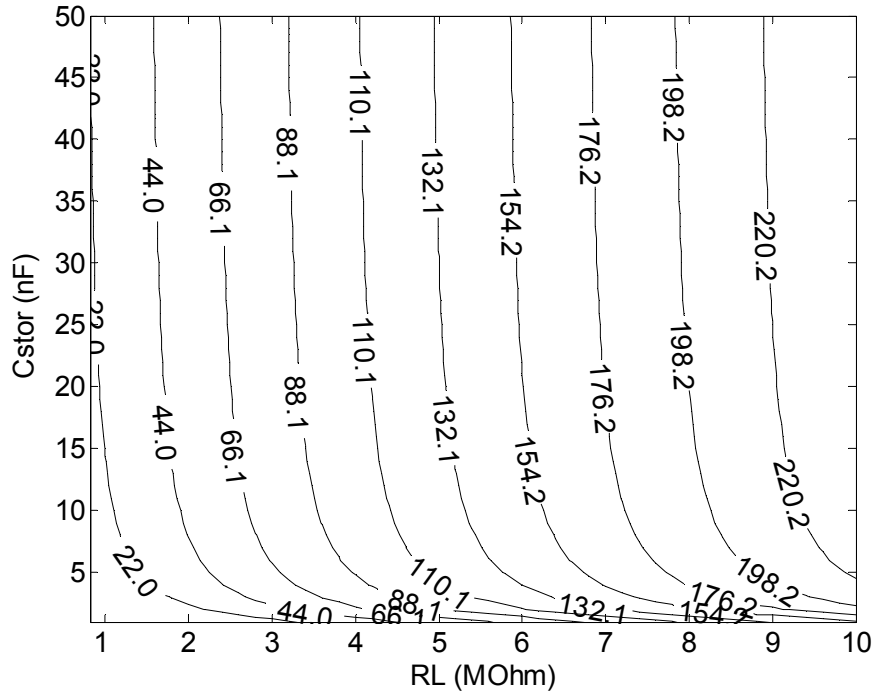


Figure 2.8 Output power ( $\mu\text{W}$ ) for various  $R_L$  and  $C_{\text{stor}}$

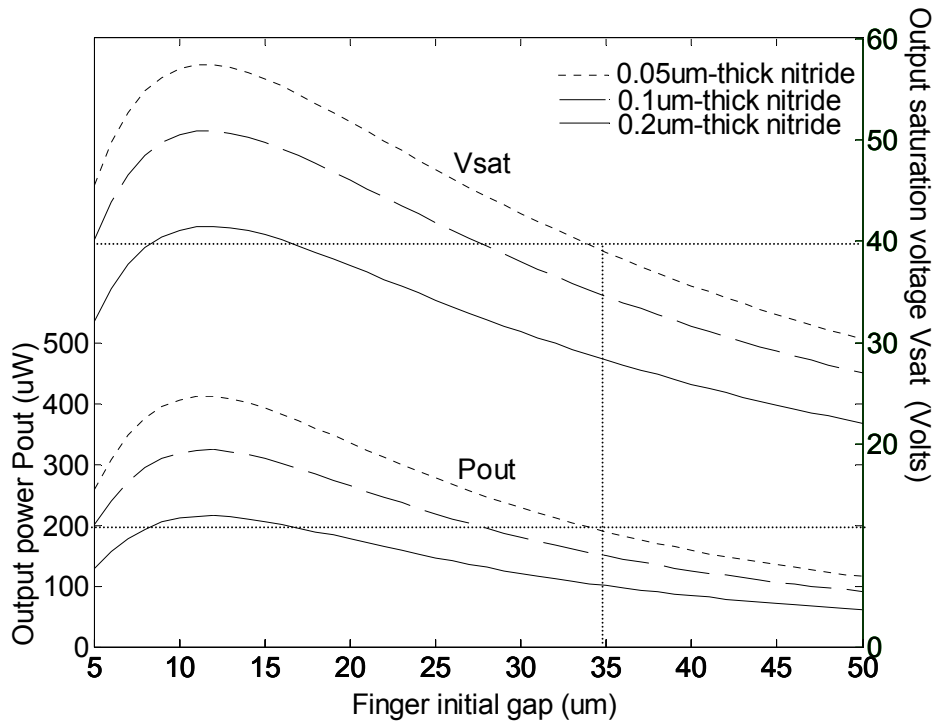


Figure 2.9 Output saturation voltage and power vs. initial finger gap ( $R_L = 8 \text{ M}\Omega$ ,  $C_{\text{stor}} = 20 \text{ nF}$ )

### 2.3.3 Dynamic analysis

After the dimension of the variable capacitor is determined from the static analysis, the dynamics of the microstructure is analyzed so that the desired maximum displacement, and hence  $C_{max}$ , can be achieved by the target vibration source. The electro-mechanical dynamics of the converter can be modeled as a spring-damper-mass system, as shown in Figure 2.10.

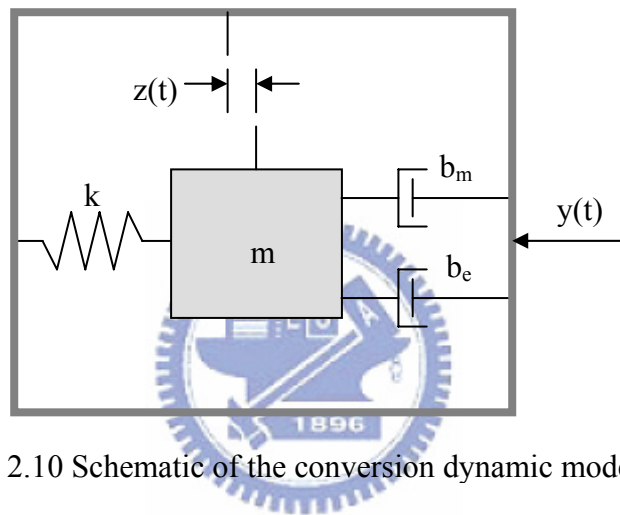


Figure 2.10 Schematic of the conversion dynamic model

The dynamic equation is

$$m\ddot{z} + b_e z + b_m(z)\dot{z} + kz = -m\ddot{y}, \quad (2.18)$$

where  $y$  is the displacement of the device frame caused by vibration,  $z$  is the displacement of the shuttle mass  $m$  with respect to the device frame,  $k$  is the spring coefficient,  $b_m(z)\dot{z}$  is the equivalent mechanical damping force representing energy loss caused mainly by the squeezed film effect, and  $b_e z$  is the electrostatic force acting on the MEMS structure discussed before in Section 2.3.1. Notice that the mechanical damping force,  $b_m(z)\dot{z}$ , is a function of both the displacement  $z$  of the shuttle mass and its velocity  $\dot{z}$  [3].

In Equation 2.18,  $b_m(z)$  and  $b_e$  are functions of  $z$ . Therefore the system is

nonlinear. In order to simplify the design, linear systems with fixed coefficients determined by the range of  $b_m(z)$  and  $b_e$  are used to approximate the original system. Fourier transform is then applied to find the trend of system behavior. The vibration source is assumed to be sinusoidal with complex amplitude  $\tilde{Y}$  and frequency  $\omega$ . With the system operated in sinusoidal steady state, Equation 2.18 reduces to

$$-m\omega^2\tilde{Z}+j\omega b_m\tilde{Z}+(k+b_e)\tilde{Z}=-m\omega^2\tilde{Y}, \quad (2.19)$$

where  $\tilde{Z}$  is the complex amplitude of  $z$ . Solving  $\tilde{Z}$ :

$$|\tilde{Z}| = \frac{m\omega^2}{\sqrt{(k+b_e-m\omega^2)^2+b_m^2\omega^2}}|\tilde{Y}|, \quad (2.20)$$

Notice that the denominator in Equation 2.20 is minimized if the term  $(k+b_e-m\omega^2)^2$  is set to zero, e.g.  $k+b_e-m\omega^2=0$ , and thus the displacement  $\tilde{Z}$  is maximized. In other words, the resonant frequency of the spring mass system  $\sqrt{\frac{k+b_e}{m}}$  must match the driving frequency. Nevertheless, because of the charging and discharging process on the variable capacitor, the charge  $Q$  carried on the variable capacitor is not a constant, and neither is the resulting  $b_e$  (since  $b_e$  is equal to  $\frac{-Q^2}{2N_g d\epsilon_0 L_r h}$ ). In fact, the calculation shows that  $b_e$  varies from -59 to -9124  $\mu\text{N}/\mu\text{m}$ . Substituting  $120 \times 2\pi$  for  $\omega$  and solving

$$\omega = \sqrt{\frac{k+b_e}{m}}, \quad (2.21)$$

a range for the relationship between optimal  $k$  and  $m$  is obtained:

$$k-567913m=59 \sim 9124 \text{ (}\mu\text{N}/\mu\text{m)}. \quad (2.22)$$

This range is helpful for us to choose appropriate attached mass  $m$  and corresponding spring constant  $k$  later in this section.

A Simulink model was built to simulate the system behavior based on Figure 2.4

(a) and Equation 2.18, as shown in Figure 2.11. The charge redistribution box calculates the charging and discharging events when  $C_v$  reaches  $C_{max}$  or  $C_{min}$ . This process represents the power output. Due to the limited shuttle mass that can be achieved in a MEMS process using only silicon, an external attached mass  $m$  is considered in order to increase the displacement of the variable capacitor and the energy conversion efficiency.

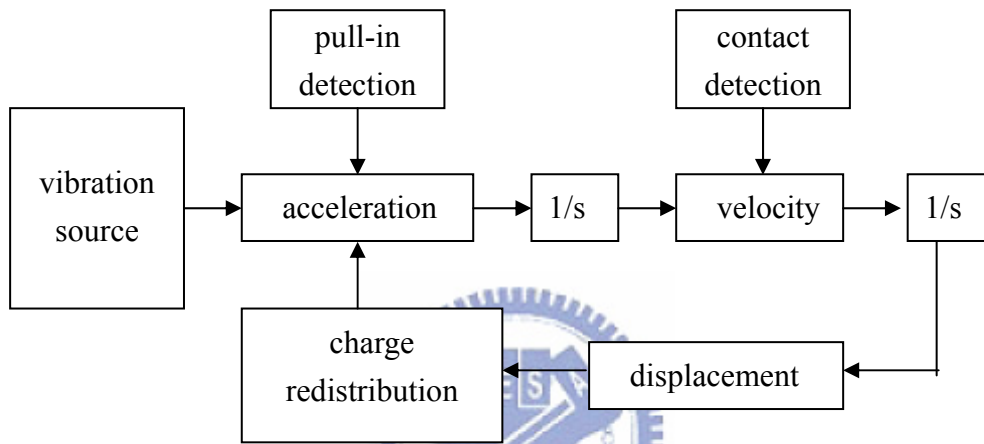


Figure 2.11 Dynamic simulation diagram

According to Equation 2.22, various attached mass  $m$  and corresponding spring constant  $k$  are chosen to simulate the maximum achievable displacement. As shown in Figure 2.12, a mass of 7.2 gram is required to achieve the maximum 34.8  $\mu\text{m}$  displacement according to the static design. The corresponding spring constant is 4300  $\mu\text{N}/\mu\text{m}$ . With these values, the output voltage simulated by the Simulink model as a function of time is plotted in Figure 2.13. The charging-discharging cycles are evident and the saturation voltage  $V_{sat}$  is close to the expected value of 40 V. Table 2.1 summarizes the important device parameters according to both the static and dynamic analyses. The device thickness  $h$ , length of finger  $L_f$ , width of finger  $W_f$ , and initial finger gap  $d$  are shown in Figure 2.14.

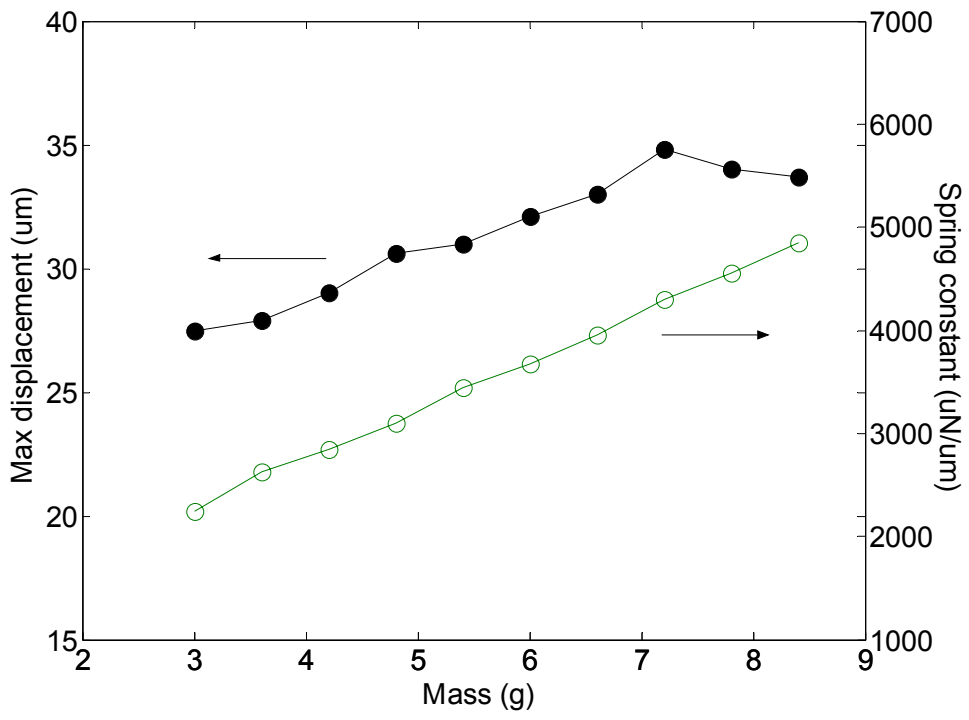


Figure 2.12 Maximum displacement and spring constant for various attached mass

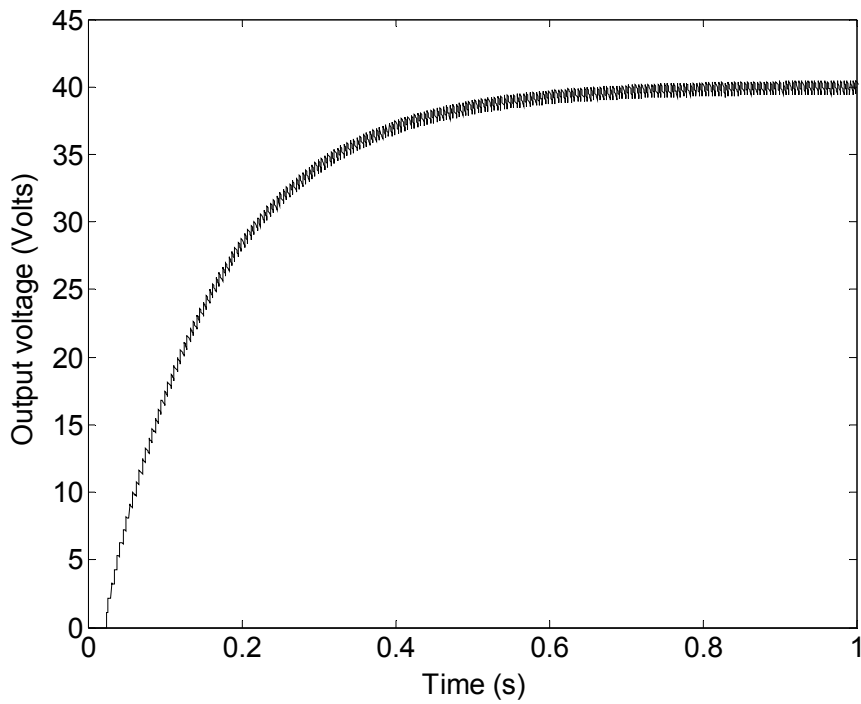


Figure 2.13 Output voltage vs. time

Table 2.1 Design parameters of the energy converter

Parameter	Description	
W	Width of shuttle mass	10 mm
L	Length of shuttle mass	8 mm
h	Device thickness	200 $\mu\text{m}$
$L_f$	Length of finger	1200 $\mu\text{m}$
$W_f$	Width of finger	10 $\mu\text{m}$
m	Shuttle mass	7.2 gram
d	Initial finger gap	35 $\mu\text{m}$
$d_{\text{min}}$	Minimum finger gap	0.1 $\mu\text{m}$
$C_{\text{stor}}$	Storage capacitance	20 nF
k	Spring constant	4300 $\mu\text{N}/\mu\text{m}$
t	Dielectric layer thickness	500 $\text{\AA}$
$\epsilon_r$	Dielectric constant	7 (SiN)
$R_L$	Load resistance	8 $\text{M}\Omega$
$V_{\text{sat}}$	<b>Output voltage</b>	<b><math>\sim 40 \text{ V}</math></b>
$P_{\text{out}}$	<b>Output power</b>	<b><math>\sim 200 \mu\text{W}</math></b>

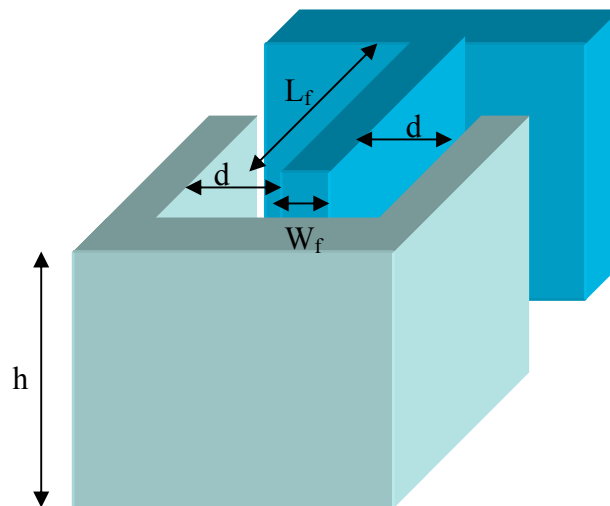
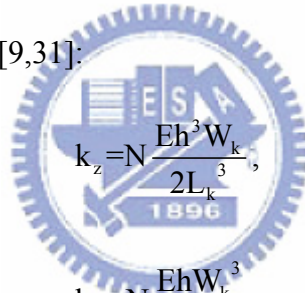


Figure 2.14 Schematic of a pair of finger gaps

The shuttle mass  $m$  and the spring constant  $k$  are determined from the dynamic analysis in the previous section. The 7.2-gram shuttle mass is huge in MEMS and can not be achieved even using SOI wafers. As a result, a high-density material such as tungsten (W) or steel should be attached to adjust the mass.

### 2.3.4 Spring design

Since the shuttle mass is extraordinary large, the out of plane elasticity can influence the reliability of the system. For the folded beam structure in Figure 2.15, the beams are anchored on the side of the device and the trusses allow expansion or contraction of the springs along the x-axis. Assuming rigid trusses, the spring constants in the three axes are [9,31]:



$$k_z = N \frac{Eh^3 W_k}{2L_k^3}, \quad (2.15)$$

$$k_x = N \frac{EhW_k^3}{2L_k^3}, \quad (2.16)$$

$$k_x = N \frac{EhW_k}{2L_k}, \quad (2.17)$$

where  $N$  is the number of springs,

$h$  is thickness of spring ( $=200 \mu\text{m}$ ),

$E$  is the young's modulus of single crystal silicon ( $=169\text{GPA}$ ),

$L_k$  and  $W_k$  are the length and width of beam, and

$L_t$  and  $W_t$  are the length and width of truss.

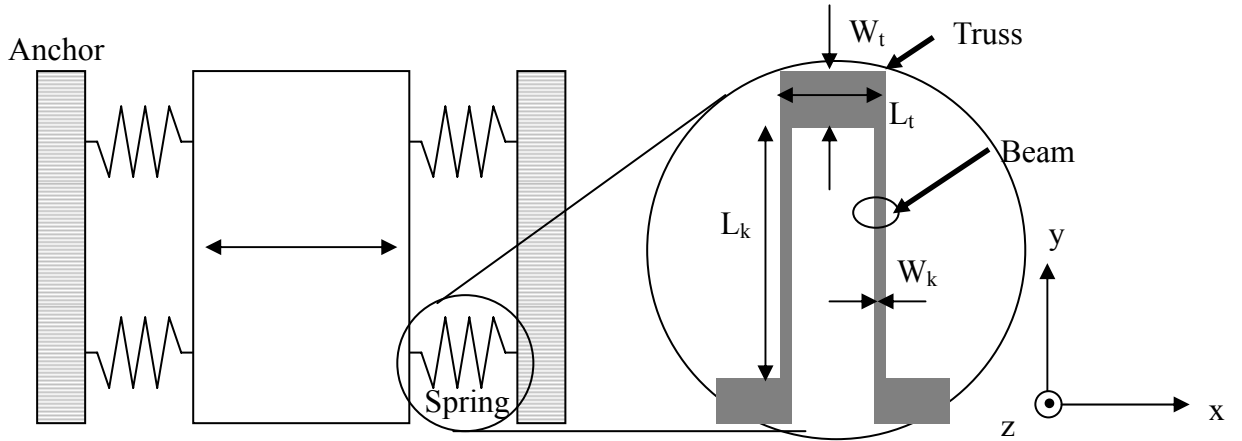


Figure 2.15 Spring structure top view

For a more extensive analysis of folded beams, including the effect of compliant trusses, the spring constants above must be multiplied by a coefficient  $\lambda$ , a function of beam and truss length and width [32]:

$$\lambda = \frac{a^2 + 16as^3 + 44s^6}{4a^2 + 34as^3 + 44s^6} \quad (2.18)$$

where  $a$  is the truss length to beam length ratio ( $L_t/L_k$ ) and  $s$  is the truss width to beam width ratio ( $W_t/W_k$ ). In our spring design,  $L_t=50 \mu\text{m}$ ,  $L_k=328 \mu\text{m}$ ,  $W_t=25 \mu\text{m}$  and  $W_k=10 \mu\text{m}$ . Hence,  $a$  and  $s$  are 0.1524 and 2.5, respectively. The calculated  $\lambda$  is equal to 0.996, which implies the effect of compliant trusses can be ignored.

Several other issues should be considered. First, the vertical stiffness  $k_z$  should be at least 10 times larger than the lateral stiffness  $k_x$  to reduce out-of-axis motion. The static displacement under the weight of the proof mass,  $mg/k_z$ , is also important. Second, the yield stress for single crystal silicon is about 70 GPa. A safety factor  $S_f$  defined as the yield stress divided by the maximum stress on each axis will be helpful in checking the robustness of the spring. The maximum stress due to the lateral displacement and the static vertical loading of the proof mass are given

$$\sigma_x = \frac{3EW_k x_{\max}}{2L_k^2} \quad (2.19)$$



$$\sigma_z = \frac{3mgL_k}{NW_k h^2}, \quad (2.20)$$

where  $x_{\max}$  is the maximum lateral displacement.

There are 8 springs, 4 on each side of the shuttle plate, and the resonant frequency is 123 Hz. The maximum lateral stress is 0.92 GPa when the maximum displacement is 34.8  $\mu\text{m}$ . The vertical stress is 21.7 MPa with mass  $m=7.2$  g. The resulting axial and vertical static safety factors are  $Sf_x=76.08$  and  $Sf_z=3225.8$ , respectively. The spring constant  $k_x$  is 4300  $\mu\text{N}/\mu\text{m}$ , which is far below the other two spring constants. The final devices parameters of the springs are listed in Table 2.2.

Table 2.2 Spring design and safety factor

Variable	Description of variables	
h	Thickness of spring	200 $\mu\text{m}$
N	Spring number	8
$W_k$	Spring Width	10 $\mu\text{m}$
$L_k$	Spring Length	328 $\mu\text{m}$
$k_z$	Vertical spring constant	$1.72 \times 10^6 \mu\text{N}/\mu\text{m}$
$k_x$	X-axis spring constant	4300 $\mu\text{N}/\mu\text{m}$
$k_y$	Y-axis spring constant	$4.63 \times 10^6 \mu\text{N}/\mu\text{m}$
$k_z / k_x$	Vertical to lateral spring ratio	400
$k_y / k_x$	Non-axial to axial spring ratio	1077
$Sf_x$	Safety factor - axial	76.08
$Sf_z$	Safety factor - vertical static	3225.8

Modal analysis is performed by Coventorware. The result shows that the first mode is the lateral mode with resonance frequency of 110 Hz. The second mode is the tilt mode with resonance frequency of 245 Hz. The second mode frequency is more

than twice of that of the first mode, which is quite safe in this application. The equivalent lateral spring constant ( $3704 \mu\text{N}/\mu\text{m}$ ) is smaller than calculated. However, the shift in resonant frequency due to spring modeling can be compensated by adjusting the external load mass.

### 2.3.5 Layout design

Mechanical stops are designed on the anchor. The fixed fingers are electrically connected. The center hole on the movable plate is for the positioning of the attached mass (a steel ball or a battery cell). The size of the center hole is designed to keep the attached mass from touching the underneath substrate.

The overall layout schematic is shown in Figure 2.16. Compared to previous layout (Figure 2.17) [27], more fingers are inserted into the center plate to increase the variable capacitance by 50%.

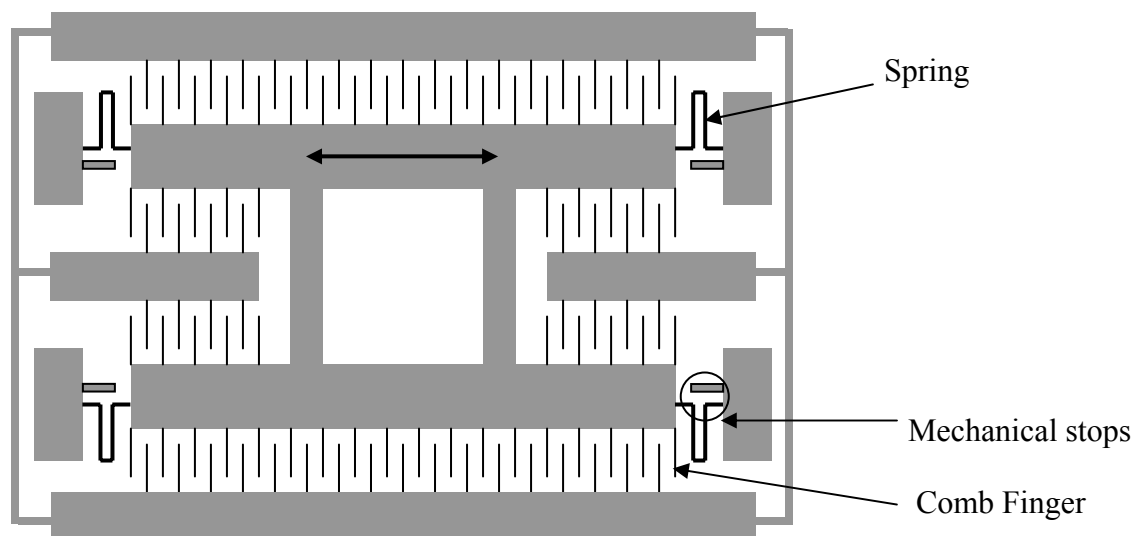


Figure 2.16 Schematic of the current device

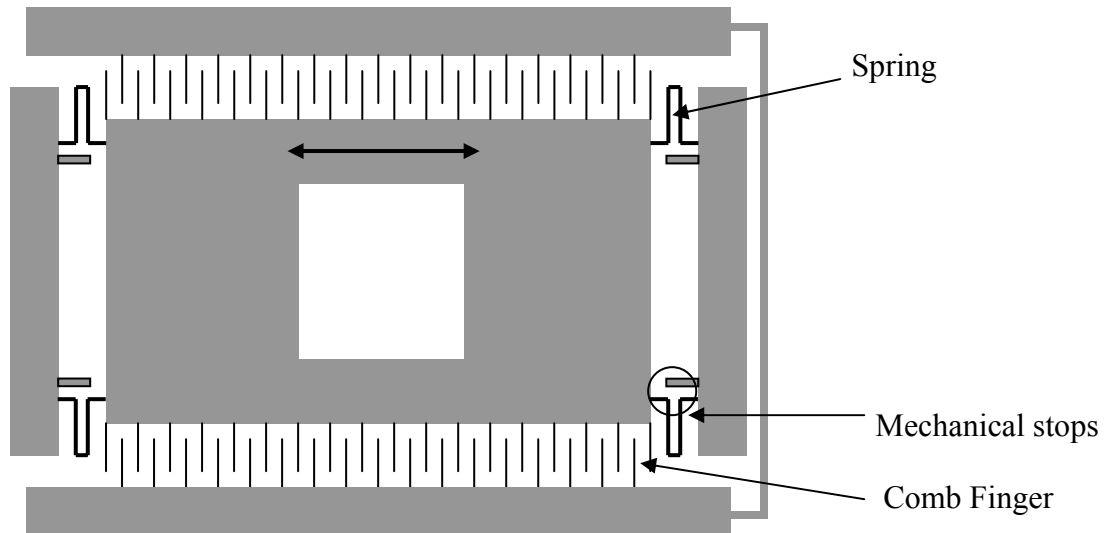


Figure 2.17 Schematic of the previous device

## 2.4 Circuits and energy storage

In this section, the circuit used to measure the power output and the devices used to store converted energy are discussed.



### 2.4.1 Measurement circuits

In the original design, the entire device including circuits should be test and measured according to the schematic shown in Figure 2.4(a). A similar prototype with a measurement circuit (Figure 2.18) was tested by Roundy [9].

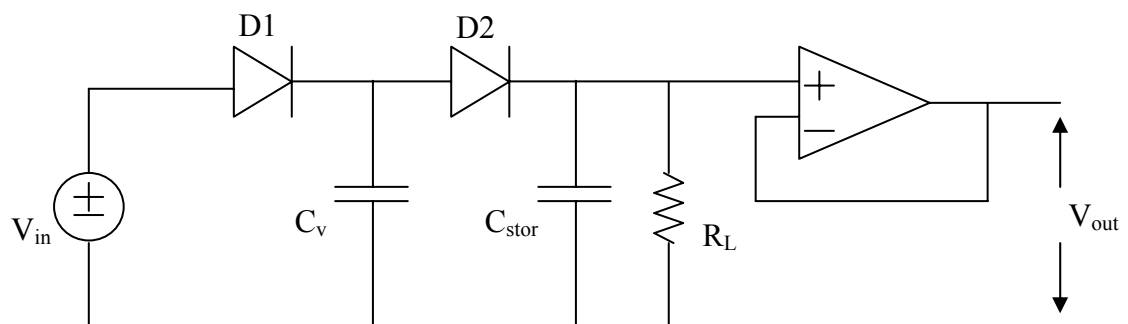


Figure 2.18 Measurement circuit by Roundy

However, the prototype fabricated by Roundy was not functional due to the reverse leakage current of diodes. In fact, reverse leakage currents of commercially available diodes (range from about 1  $\mu\text{A}$  to about 100  $\mu\text{A}$ ) are often too large. For a capacitor of about 100 pF (the order of  $C_{\min}$ ), a 1  $\mu\text{A}$  leakage current will result in a 10000 V/s voltage drop. In our design, the circuit is operating at 240 Hz (two times of the vibration frequency), which means each cycle lasts for 4.16 ms and the voltage drop will be 41.6 V, which is too large. Thus another circuit model with an AC current output as shown in Figure 2.19 is proposed [27]. For a DC voltage source  $V_{\text{in}}$  such as battery, the serial variable capacitor will induce an AC current  $I(t)$  at the output port. Since DC current is blocked by the capacitor, there is no net power output from the voltage source. Thus the output power of this circuit is purely derived by the driving vibration.

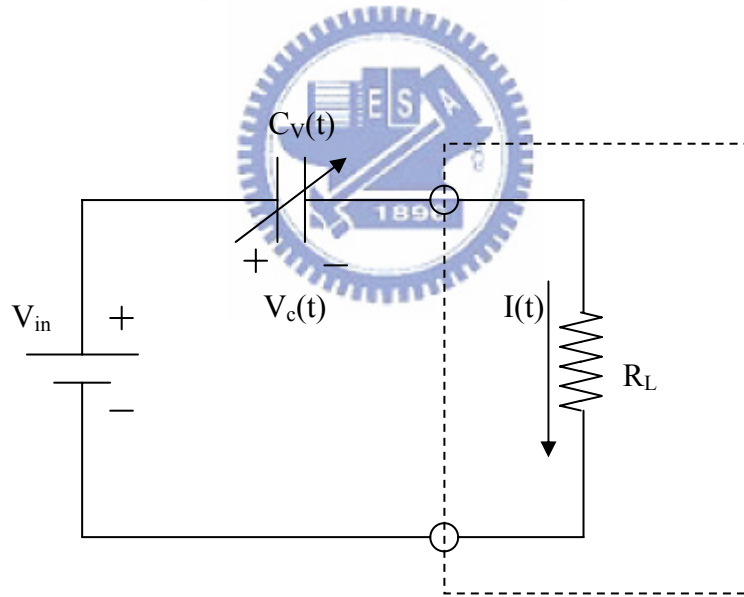


Figure 2.19 Modified circuit schematic

Based on the modified circuit, the equations below can be derived:

$$V_{\text{in}} = V_c(t) + I(t) \times R_L, \text{ and} \quad (2.21)$$

$$\text{and } I(t) = \frac{dQ(t)}{dt} = \frac{d[C_v(t)V_c(t)]}{dt}. \quad (2.22)$$

Equation 2.22 can be simulated by a Simulink model. Assuming the displacement  $Z(t)$

is sinusoid with an amplitude of  $34.8 \mu\text{m}$ , the AC output current is about  $15 \mu\text{A}$  (Figure 2.20) for a  $3.3 \text{ V}$  input voltage and  $10 \text{ k}\Omega$  load resistance. Therefore, the output power is about  $1.1 \mu\text{W}$ .

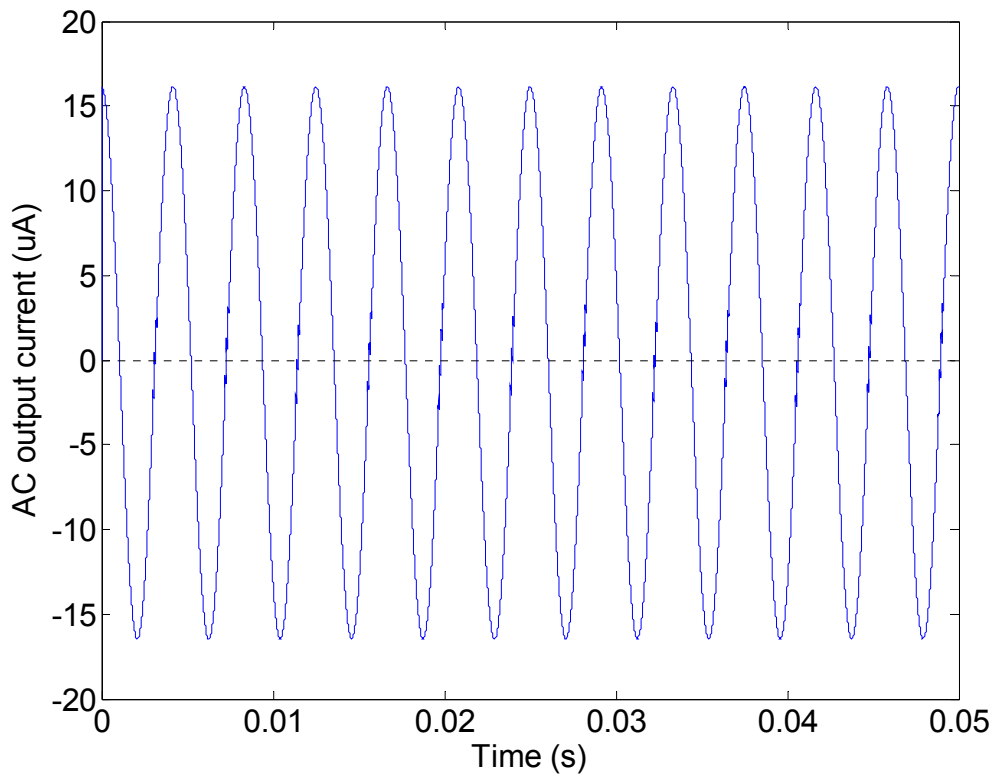


Figure 2.20 AC output current

## 2.4.2 Storage device

When energy converters do not supply energy continuously for most of the time, a good solution is to store the converted energy, which means to convert energy in storage elements in order to provide power and energy more smoothly. Typical storage devices include capacitors, inductors, and batteries.

Capacitors and inductors have lower energy density. They often serve as intermediate and short-term energy storage cells because they are less sensitive to leakage. Batteries, such as NiZn, NiMH, NiCd, and Lithium-ion (Li-ion) store energy

chemically and are rechargeable. Among these kinds of batteries, Li-ion batteries (Figure 2.21) offer best characteristics with higher energy density and discharge rate, higher cell voltage, longer cycle life, and nonexistent “memory” effects. The only drawback is Li-ion batteries are too sensitive to over charging and discharging. Charging them above 4.2 V or higher, or discharging them below 2.7 V will damage the batteries and make them vent or explode [33]. In this study, LIR1620 (3.6V,  $\Phi$ 16mm, H2.2mm, 1.2g) and LIR2016 (3.6V,  $\Phi$ 20mm, H1.8mm, 1.6g) Li-ion cells can be used to store converted energy. Moreover, the battery is able to contribute a part of mass needed if it is well bonded on the device.



Figure 2.21 Lithium-ion rechargeable battery

## 2.5 Conclusion

A micro electrostatic vibration-to-electricity energy converter is designed in this chapter. For the 3.3 V supply voltage and 1cm<sup>2</sup> chip area constraints, optimal device parameters were found from theoretical calculation and Simulink simulation. In the current design, the output power is 200  $\mu$ W/cm<sup>2</sup> for the optimal load of 8 M $\Omega$ . The device structures such as the variable capacitor and springs are also discussed.

## Chapter 3 Fabrication Process

Processes to fabricate the variable capacitors described in Chapter 2 using MEMS fabrication technology are discussed. SOI wafers are used due to the large device thickness and therefore large capacitance. Additionally, deep reactive ion etching (DRIE) processes are used to fabricate devices with high aspect ratios to maximize capacitance. A further benefit of the thick device layer and high aspect ratio is that the resulting devices have a very large out-of-plane stiffness compared to the in-plane stiffness. This is important for the attachment of a significant amount of mass to the device after the fabrication process is completed. Finally, our previous work [27] showed that the substrate beneath the device was the major contribution to parasitic conductance and the stiction problem. Therefore, backside etching by DRIE is also included in the new process.

The proposed processes rely heavily on DRIE, which causes various problems. After the entire process flow, only a few devices survived. Explanations for some of the problems in the fabrication as well as proposed solutions will be discussed.

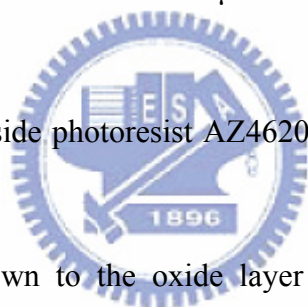
### 3.1 Process flow

Since the device is relatively large, the device layer should be highly conductive to reduce resistive losses. Thus the resistivity of the device layer is less than 0.02  $\Omega$ -cm. Parasitic capacitance caused by the substrate is reduced by removing the substrate under the center plate by backside etching. Though the backside etching does increase the processing complexity, the stiction in the releasing step can be prevented thereby. However, since the area of the etched substrate is very large, the

robustness of the wafer or die can be a problem. The width of the outer frame, which also serves as the electrode of the fixed finger, are extended to 2.5 mm to strengthen the support of the device and the attached mass.

Most of the fabrication was conducted in the Nano Facility Center at National Chiao-Tung University and the Nano Science and Technology Center at National Tsing-Hua University. The basic processing steps are illustrated in Figure 3.1 and discussed in the following.

- (a) Start from a double-side polished P-type  $\langle 100 \rangle$  SOI wafer with a device layer of 200  $\mu\text{m}$ , oxide layer of 5  $\mu\text{m}$ , and handle layer (substrate) of 400  $\mu\text{m}$ . The resistivity of the device layer is less than 0.02  $\Omega\text{-cm}$ .
- (b) Spin coat a thick photoresist AZ4620 of 6  $\mu\text{m}$  on the wafer backside and pattern via photolithography.
- (c) Coat and pattern the frontside photoresist AZ4620 of 6  $\mu\text{m}$  using the double side aligner.
- (d) Etch the device layer down to the oxide layer to form fingers, springs, and movable plates using DRIE.
- (e) Etch the backside to form the outer frame and the dividing gap by DRIE.
- (f) Remove photoresist and deposit silicon nitride on the finger side walls by low pressure chemical vapor deposition (LPCVD).
- (g) Etch the top layer of silicon nitride on the frontside by reactive ion etching (RIE).
- (h) Etch the 5- $\mu\text{m}$ -thick sacrificial oxide from backside by RIE to release the movable parts.
- (i) Coat aluminum of less than 5000  $\text{\AA}$  to form the pad contact and interconnection by thermal evaporation. After this step, the wafer is cleaved manually and wire bonding is conducted.
- (j) Attach the external mass to the movable plate.





The DRIE etcher used in the fabrication process is an Alcatel AMS100 etcher using the standard Bosch process. Passivation is achieved by  $C_4F_8$ , and silicon etching by  $SF_6$ .

After the DRIE in step (g), the remaining photoresist are removed by oxygen plasma in the RIE chamber. The 5- $\mu\text{m}$ -thick sacrificial oxide was then etched by  $CHF_3$  and  $SF_6$  for about 65~70 minutes. The oxide etching time should be controlled carefully to avoid overetching and destroying the frontside devices.

In the dicing process (i), the cooling water often damaged fingers and caused a lot of broken pieces and shortage problems [27]. Therefore, wafer dicing was performed manually. A diamond scribe was used to cleave dies along the dividing gaps formed by DRIE.

Since the required mass is large, high density material such as tungsten or steel is used to reduce the size. In the final step of the fabrication process (step (j)), the mass needs to be placed precisely on the center of the device; otherwise the nonaxial motion will be induced. Therefore, the movable plate has a large hole in the center for a spherical ball to be fit into the position automatically. The resonant frequency can be adjusted by using balls with different diameter (and thus mass) to match the vibration frequency. The steel ball is bond to the center plate by a double stick tape.

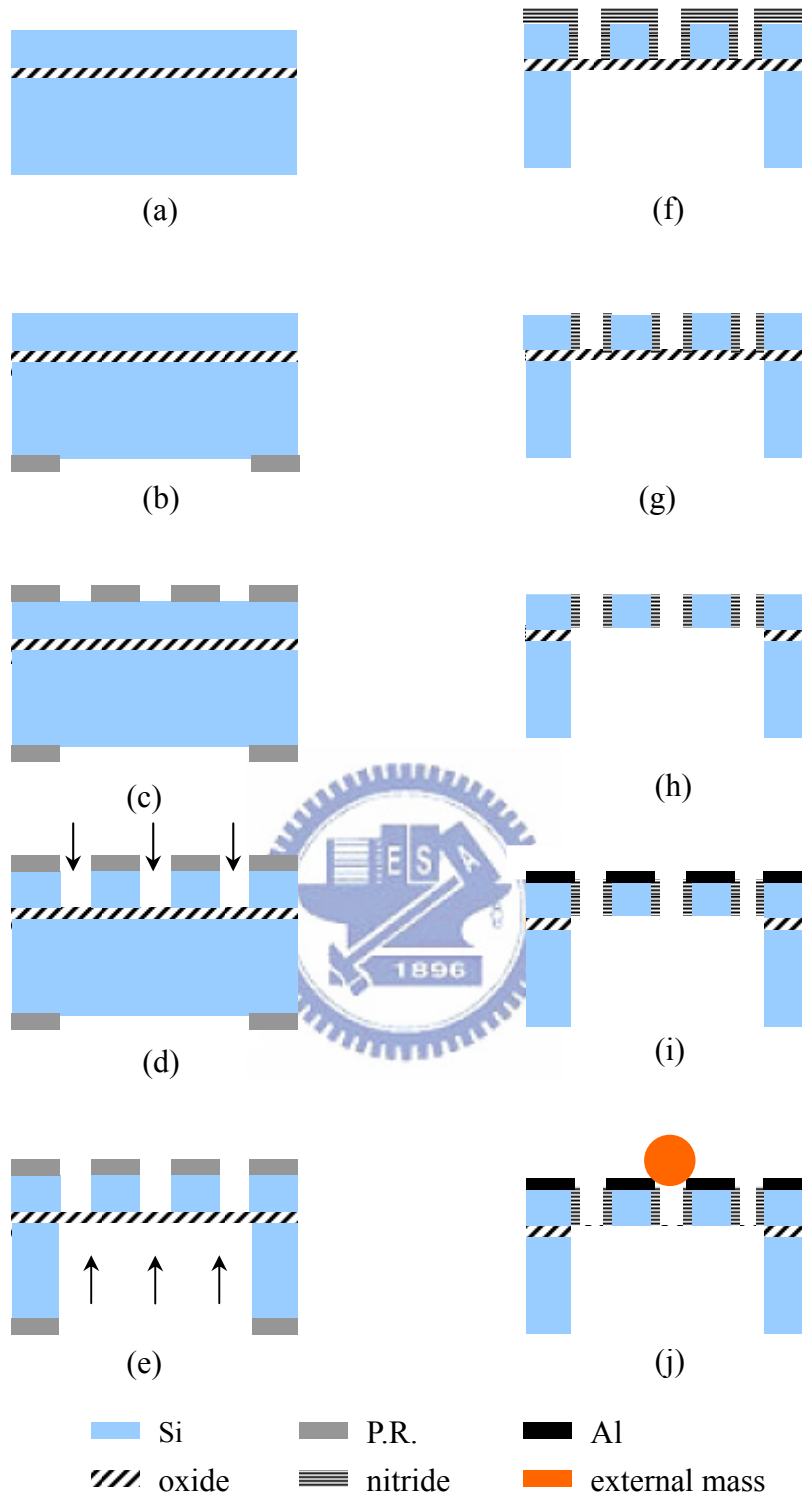


Figure 3.1 Processing steps: (a) start from a SOI wafer, (b) coat and pattern backside P.R., (c) coat and pattern frontside P.R., (d) etch the device layer by DRIE, (e) etch the backside by DRIE, (f) deposit silicon nitride on the finger side walls by LPCVD, (g) etch top silicon nitride layer on the frontside by RIE, (h) etch sacrificial oxide from backside by RIE, (i) apply Al by thermal coater, and (j) attach external mass

## 3.2 Discussion

Problems and issues found in the fabrication process are discussed. Solutions are proposed and demonstrated in this section.

### 3.2.1 Overheating of the wafers

In the first run, the backside etching was done with KOH solution before defining frontside structures by DRIE. A 6000-Å-thick LPCVD silicon nitride was first deposited on both sides of the SOI wafer as the wet etching mask. After the etching window on the backside was opened, the full wafer was immersed in the 45.8 wt% KOH solution at 80°C. The wet etching lasted for 10 hours and 45 minutes for an etching rate of 0.62  $\mu\text{m}/\text{min}$  and stopped at the sacrificial oxide layer.

However, the long wet etching caused a problem for the subsequent DRIE process. Since the edge of wafer was not completely covered by the silicon nitride film in LPCVD, the wafer was attacked by KOH from its edge when fully immersed into the solution. Consequently, it became a smaller disk than a normal 4" wafer and could not be clamped well by the mechanical chuck in the DRIE etcher. One solution was to dice the wet-etched SOI wafer into dies and then bond them to a carrier wafer. As shown in Figure 3.2, photoresist was coated on the carrier wafer to provide adhesion for dies and a heat conducting path for the cooling gas (helium) to dissipate process heat. Unfortunately, the etching was not controlled well and structures were overetched. As a result, the fingers and springs were etched sideways (Figure 3.3) and disintegrated (Figure 3.4).

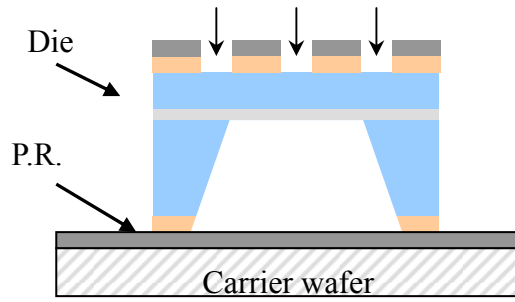
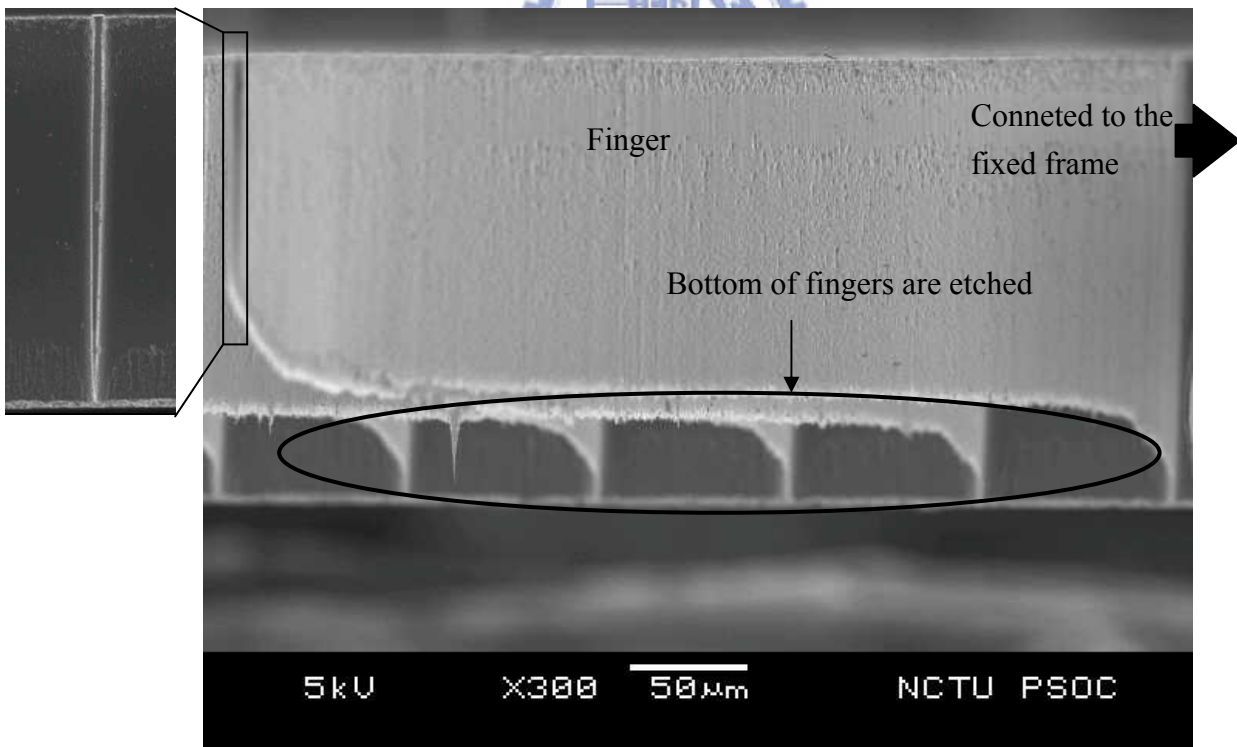
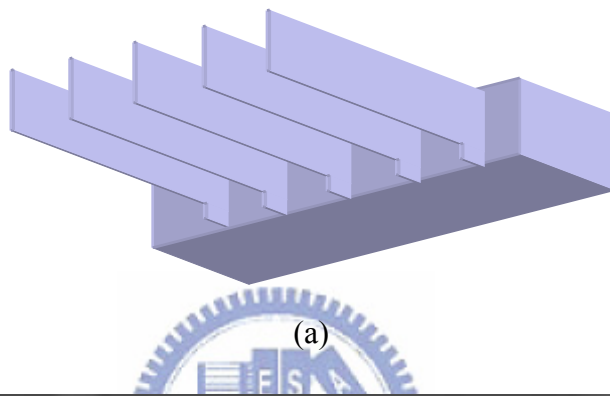


Figure 3.2 Die and carrier wafer for DRIE



(b)

Figure 3.3 Sideways etched fingers: (a) illustration and (b) sideview

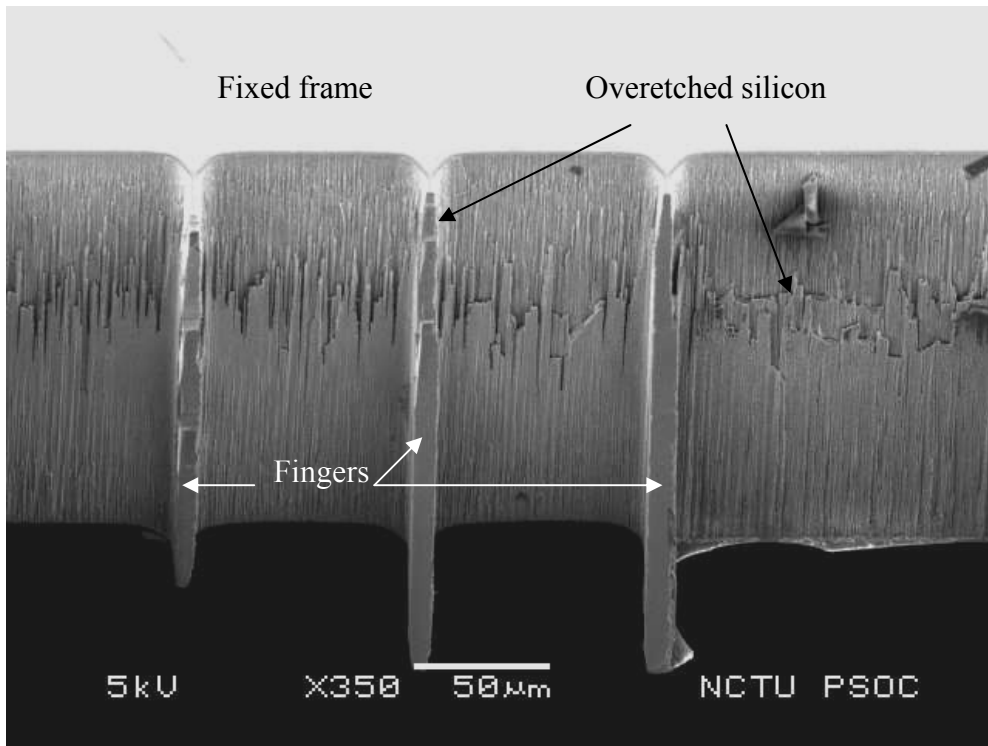


Figure 3.4 Cross section of broken fingers

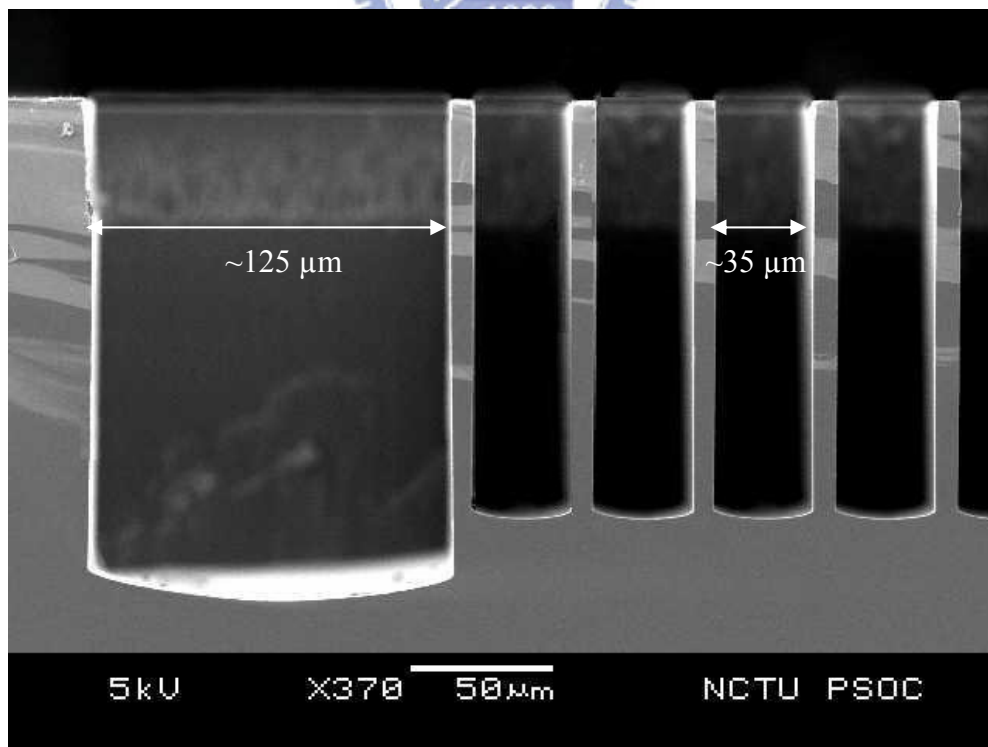


Figure 3.5 RIE lag effect

In the next try, the wet etching on the backside was replaced by DRIE. After the backside etching, the front device layer was also etched by DRIE. However, due to the RIE lag effect in dry etching, the narrow gaps between the fingers were etched more slowly than the wide hole in the center plate as shown in Figure 3.5. While the wider spaces were cleared in about 30 minutes, the narrower spaces need 10 more minutes or so. During this extra 10-minute period, the sacrificial oxide layer always broke due to its residual stress (this will be discussed later in this section). Once the oxide layer broke, helium escaped through the breach, leading to bad cooling of the wafer.

The other issue with this process is related to the heat conducting path of the suspended structures [34]. As the suspended structures were defined, all the process heat contained on the center plate must be dissipated through the thin springs. With a width of 10  $\mu\text{m}$ , the springs were too thin to transfer enough heat outside. Combined with bad wafer cooling, it caused the temperature of the center plate, springs and movable fingers to rise dramatically. Thus, the photoresist on these sections was burned. Figure 3.6 shows burned photoresist on the suspended structures and photoresist in perfect condition on the anchor. The photoresist on the suspended springs, halfway in the thermal path between the center plate and the anchor, showed some signs of burning, but not as dramatic as that on the center plate. Once the photoresist was burned, springs were not protected and thus destroyed. Therefore, no working device was yielded in this run.

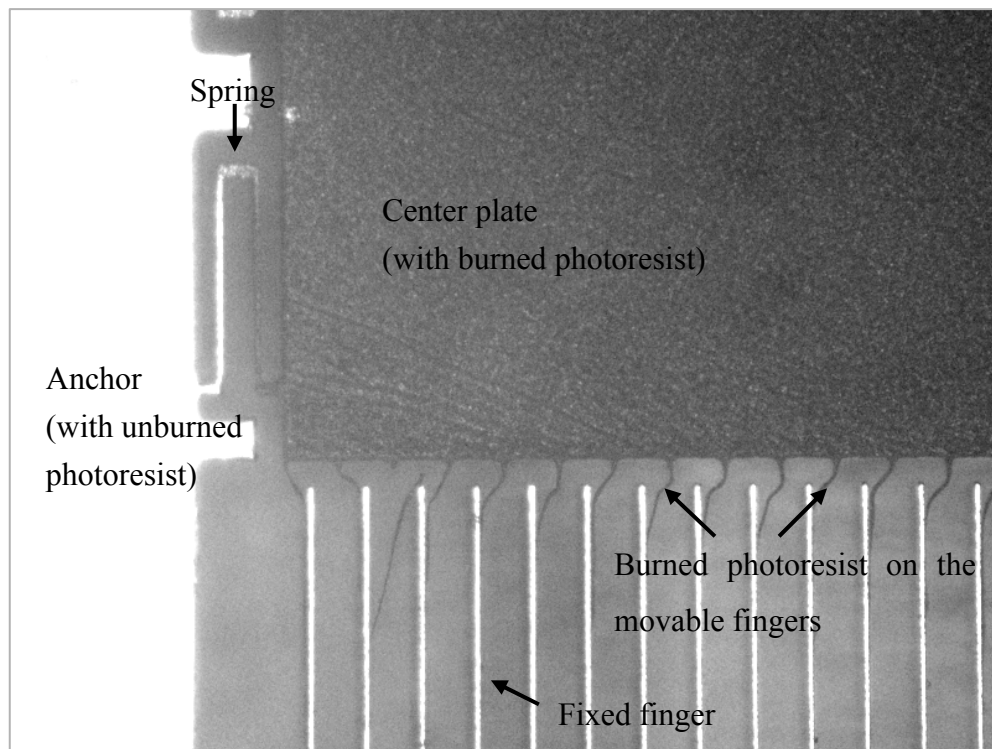


Figure 3.6 Burned photoresist due to poor cooling

In the third run, several changes were made to provide better cooling and heat conduction in the DRIE process. Although the yield was still low, a few working devices were made. The device layer was etched first, followed by the backside through-etching as shown in Figure 3.1 (d) and (e). In the backside DRIE, the regions to be etched were large openings under the suspended structures and had a uniform size. Since the etching rate depended on the size of the opening, the etching time for each block were more uniform. After the first block was opened and helium started to escape through the breach in the oxide layer, very little extra time (about 2~3 minutes) was needed to clear the other regions. As a result, the leakage of helium would not last long. Besides, since the substrates had better heat conducting path to transfer enough heat outside, there was not so much heat accumulating on the wafer and thus the problem of overheating could be alleviated.

### 3.2.2 Residual stress of the oxide layer

After the bonding process of manufacturing the SOI wafer at a high temperature, the resulting sacrificial oxide layer became stressed due to the different thermal expansion coefficients of silicon and silicon dioxide [35]. In the third run, the residual stress caused most of the springs to break. After the structures in the device layer were defined, a large area under suspended structures was removed in the backside etching. Hence, no structure was left to hold the stressed oxide layer. The oxide layer started to buckle and bent the structures in the device layer. Therefore, the most fragile parts, the springs and fingers, were broken as shown in Figure 3.7. In the future, removing the oxide layer before etching the handle layer can be helpful to eliminate this issue. Even though this may cause helium leakage, it is usually not a serious problem in backside etching. Designing a new structure with more robust springs and less etched area may also alleviate the effect of residual stress.

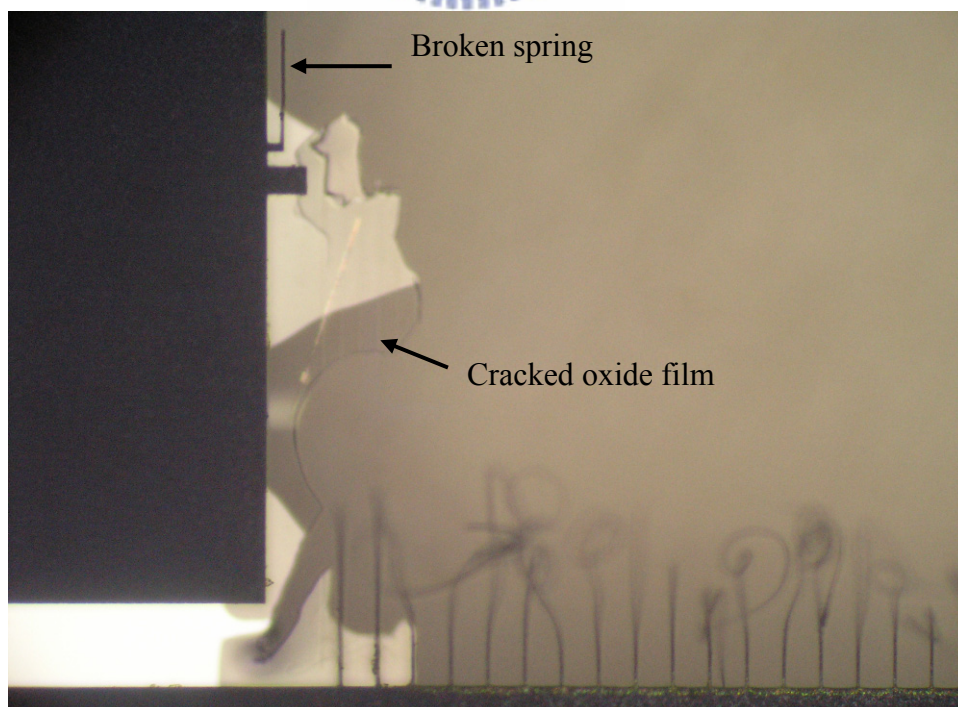


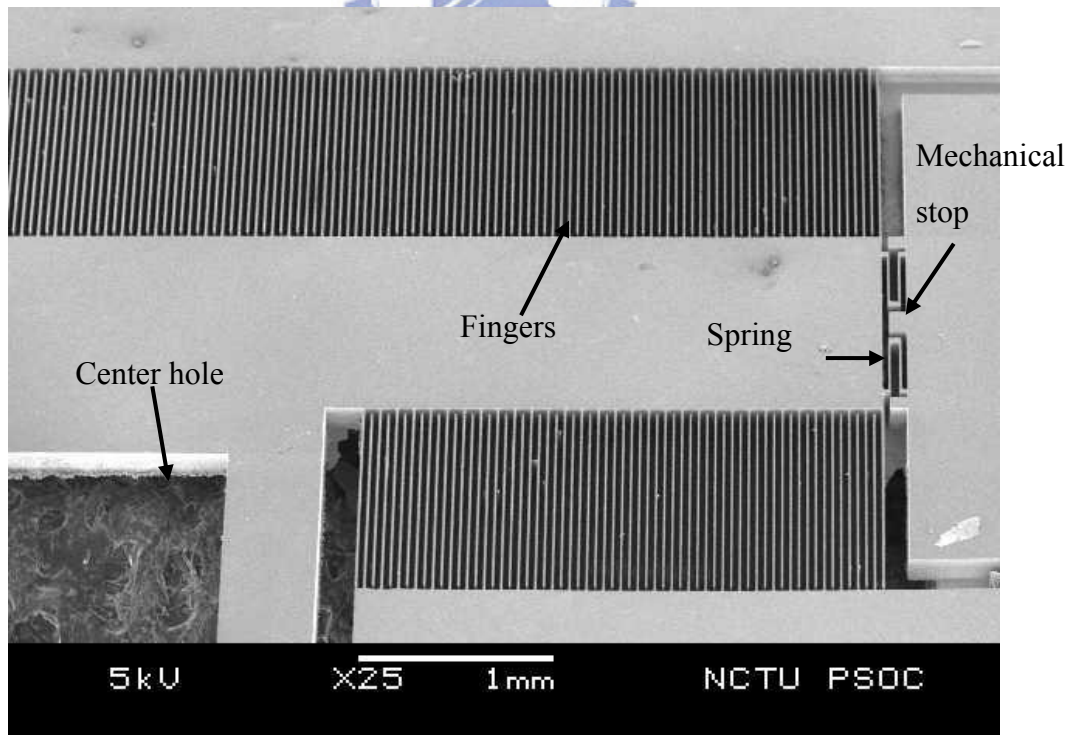
Figure 3.7 Broken structures due to residual stress



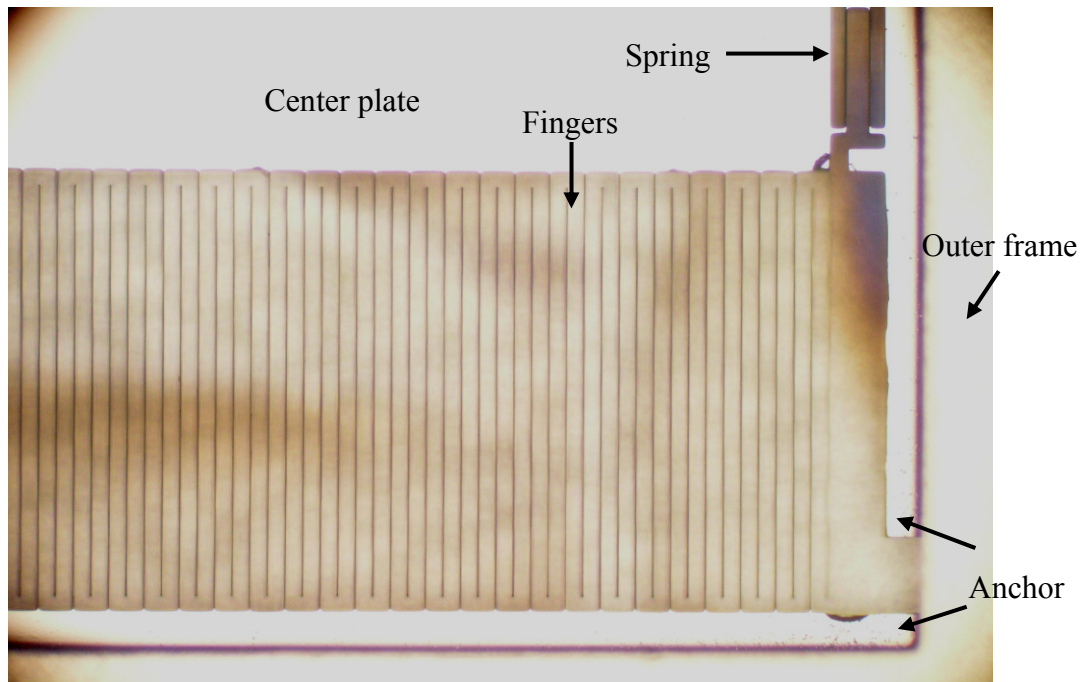
### 3.3 Fabricated device

Figure 3.8 shows the SEM photograph of a fabricated device, with the springs, fingers, mechanical stops, and the center hole for mass attachment.

With the perpendicularity about  $90^\circ$ , the fabricated fingers are  $200\ \mu\text{m}$  deep,  $1200\ \mu\text{m}$  long and about  $9.5\ \mu\text{m}$  wide, as shown in Figure 3.9. In order to yield ideal finger width of  $10\ \mu\text{m}$ , the layout finger width is pre-enlarged to  $12\ \mu\text{m}$  to compensate for the feature size shrinkage during processing. The reasons for the shrunk feature size are the non-ideal photolithography and the rise of wafer temperature in DRIE process as mentioned above. First, the cross section of patterned thick photoresist is in a tapered shape, instead of a rectangular shape due to photolithography inaccuracy, such as over exposure, over development, or the characteristic of the photoresist itself.



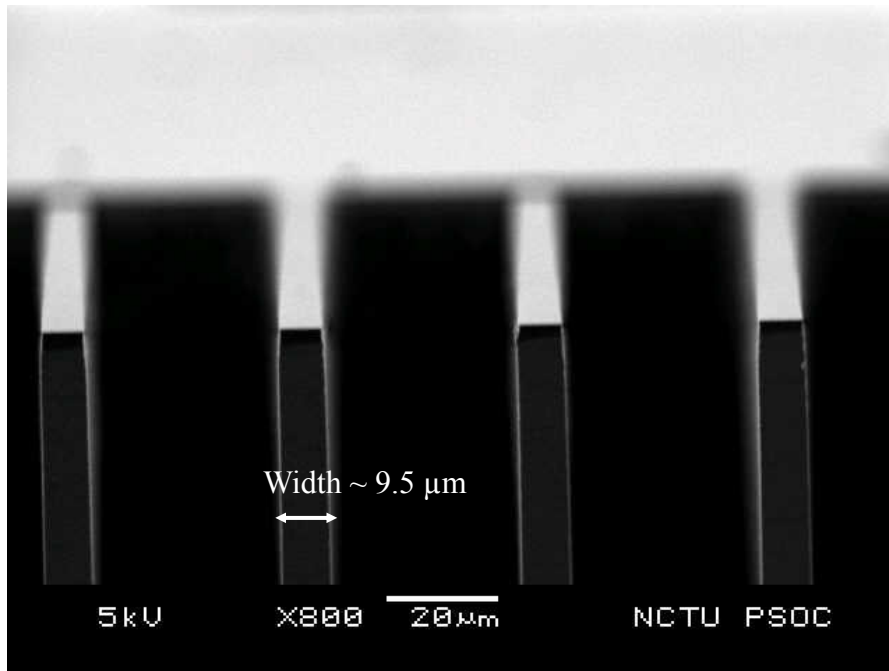
(a)



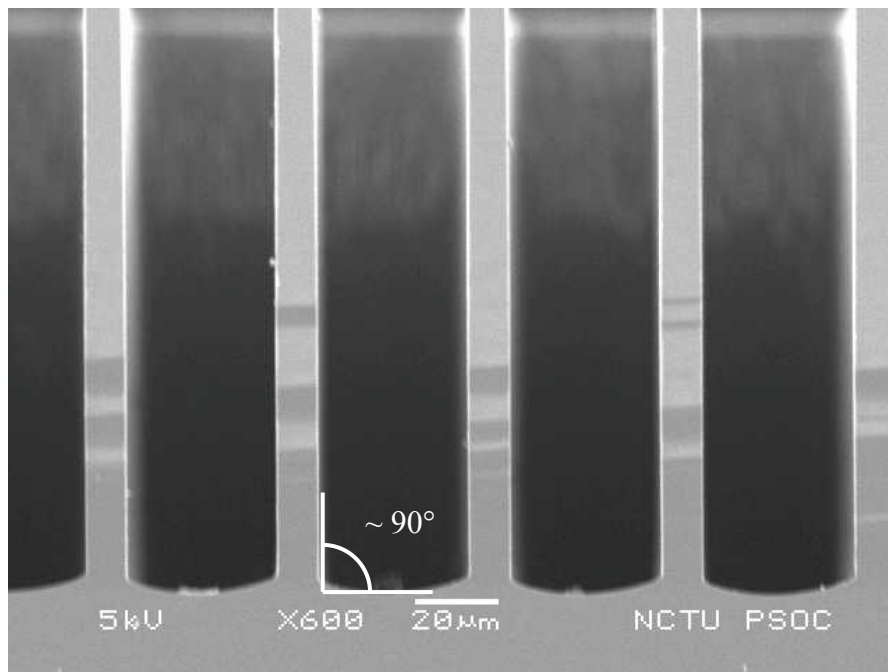
(b)

Figure 3.8 Overview of the device: (a) SEM photograph from frontside and (b) optical microscope photograph from backside

Since the photoresist serves as the hard mask for DRIE, this deviation will influence the device feature size. To improve the feature size control, thermal or PECVD oxide can be used as the hard mask, since they provide higher selectivity in DRIE and can thus maintain the ideal feature size. Second, the DRIE process is a series of etching and passivation steps. The normal processing temperature is about 45°C. When temperature increases, passivation effect is decreased. If the temperature is over 100°C, the etching becomes isotropic and thus the structures are etched sideways. Increasing the flow rate of C<sub>4</sub>F<sub>8</sub> (gas for passivation) or lengthening the time of the passivation cycle can be a solution to this problem [36].



(a)



(b)

Figure 3.9 (a) Width, (b) perpendicularity of etched fingers

In the last fabrication step, a double stick tape was first bond to the bottom of the steel ball, and then the ball is attached manually to the center plate and positioned by the center hole (Figure 3.10). This step has to be treated carefully to avoid destroying the device. The size of the total device with its outer frame is about  $0.8 \times 1.4 \times 1.7 \text{ cm}^3$ .

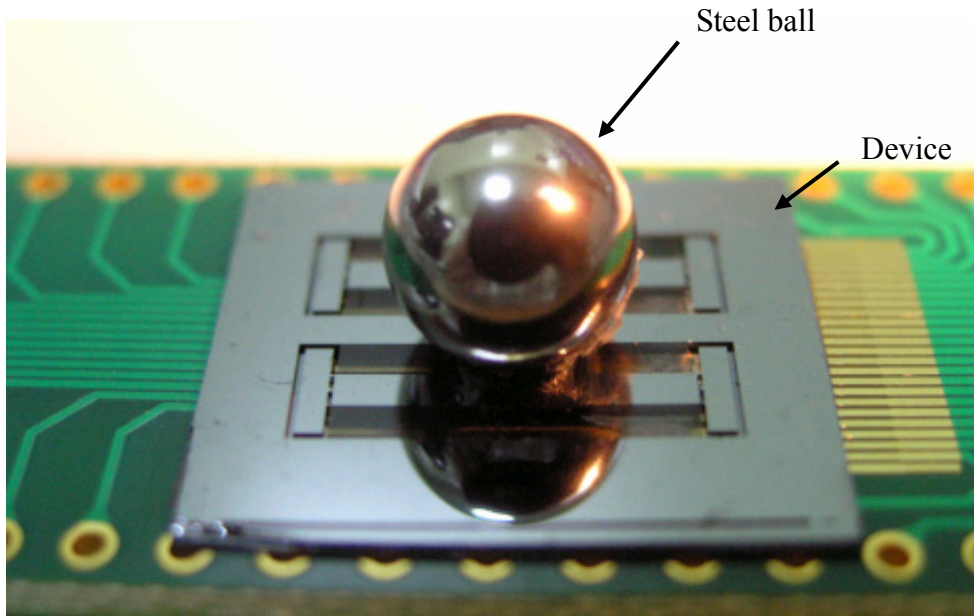


Figure 3.10 Overview of mass attachment

### 3.4 Conclusion

Our experience in the fabrication process is summarized. As discussed above, most of the issues occur in the DRIE process of SOI wafers [37].

First, when the DRIE process is necessary after the wafer is diced, the dies must be bonded to a carrier wafer by substances with high thermal conductivity, such as thermal conducting tapes or cool-grease, in order to dissipate process heat properly.

Second, even when the DRIE process is done on a full wafer, overheating can occur due to the leakage of cooling gas and poor heat dissipation of thermally isolated structures. The structure can be etched sideways when the process temperature is too high.

Third, fine structures can be broken by buckled buried oxide layer due to the residual stress. Designing a more robust structure with less etched area or pre-etching a part of the stressed oxide layer from the frontside can be helpful to protect the structure from damaging.

## Chapter 4 Device measurement

In this chapter, the measurement of the fabricated devices with various width of fingers and springs are discussed. Device displacement and resonance were observed in the mechanical measurement. In electrical measurement, the minimum and maximum capacitance are obtained. Further tests of output power and AC current are being conducted.

### 4.1 Mechanical measurement

After the devices were released, they were tested on a probe station with an optical microscope. The probes were used to push the movable parts of the device to check if they were successfully released. The other use of the probes was to remove the particles and shorted fingers.

The mechanical measurement setup is shown in Figure 4.1. The amplified sinusoidal signal was used to drive a PROWAVE JZK-1 shaker. Frequency spectra of vibration were measured by an accelerometer. The resonance of the device was observed by an optical microscope and captured by a digital camera.

The resonant frequency of devices with various spring width was measured. The fabricated spring width shrunk from 12  $\mu\text{m}$  and 10  $\mu\text{m}$  to 9.5  $\mu\text{m}$  and 6.5  $\mu\text{m}$  or 7.5  $\mu\text{m}$ , respectively. Without the attached mass, the resonant frequency ranged from 1280 to 2160 Hz as shown in Figure 4.2 (a). Since the mass of the center plate is approximately 0.017 gram, the spring constants can be estimated from the equation  $\omega = \sqrt{k/m}$ , as shown in Figure 4.3. For the ideal spring width of 10  $\mu\text{m}$ , the simulated values in Chapter 2 are about 3700  $\mu\text{N}/\mu\text{m}$ . If the feature size shrinkage is considered,

the simulated spring constants become 1020, 1560 and 3170  $\mu\text{N}/\mu\text{m}$  (Figure 4.3), which are close to the measured values.

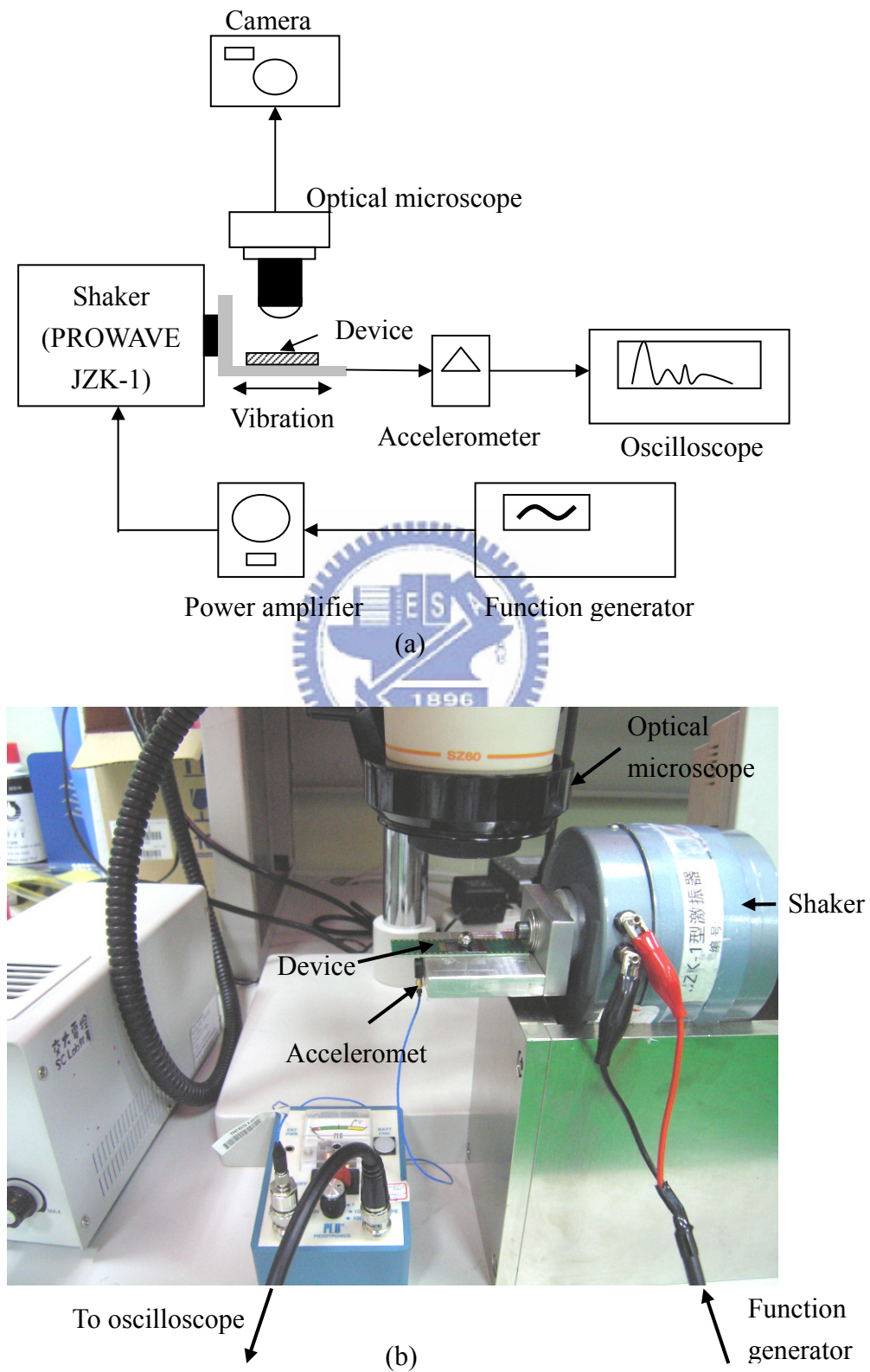


Figure 4.1 (a) Schematic and (b) photograph of the mechanical measurement setup

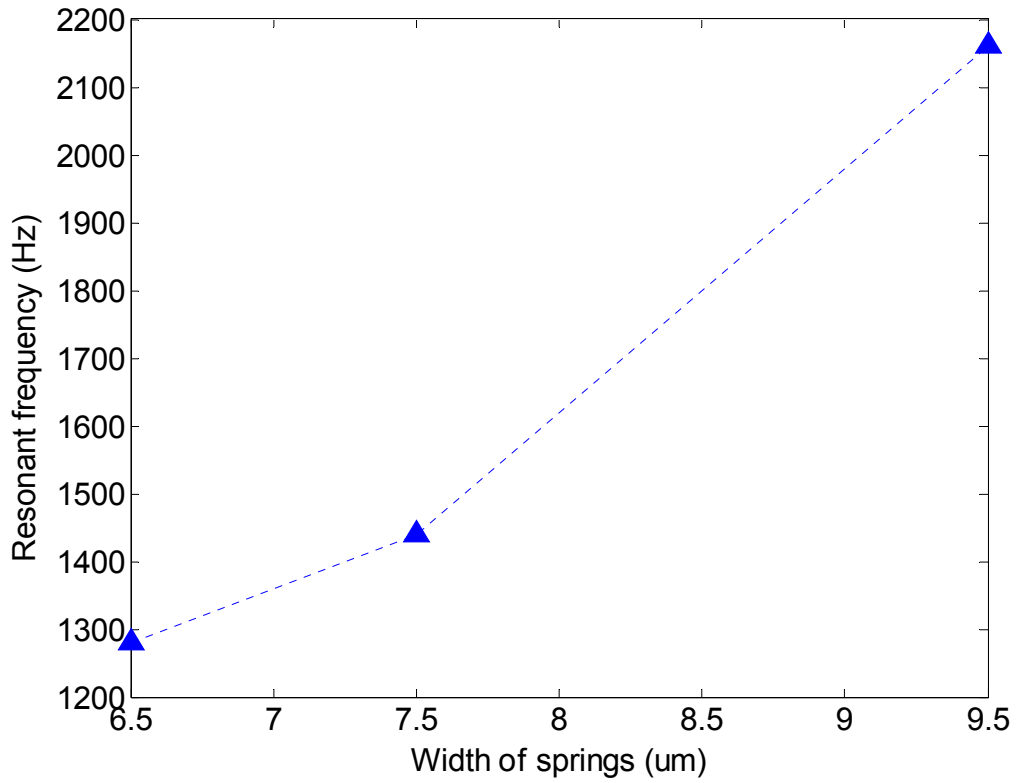


Figure 4.2 Resonant frequency with various width of springs

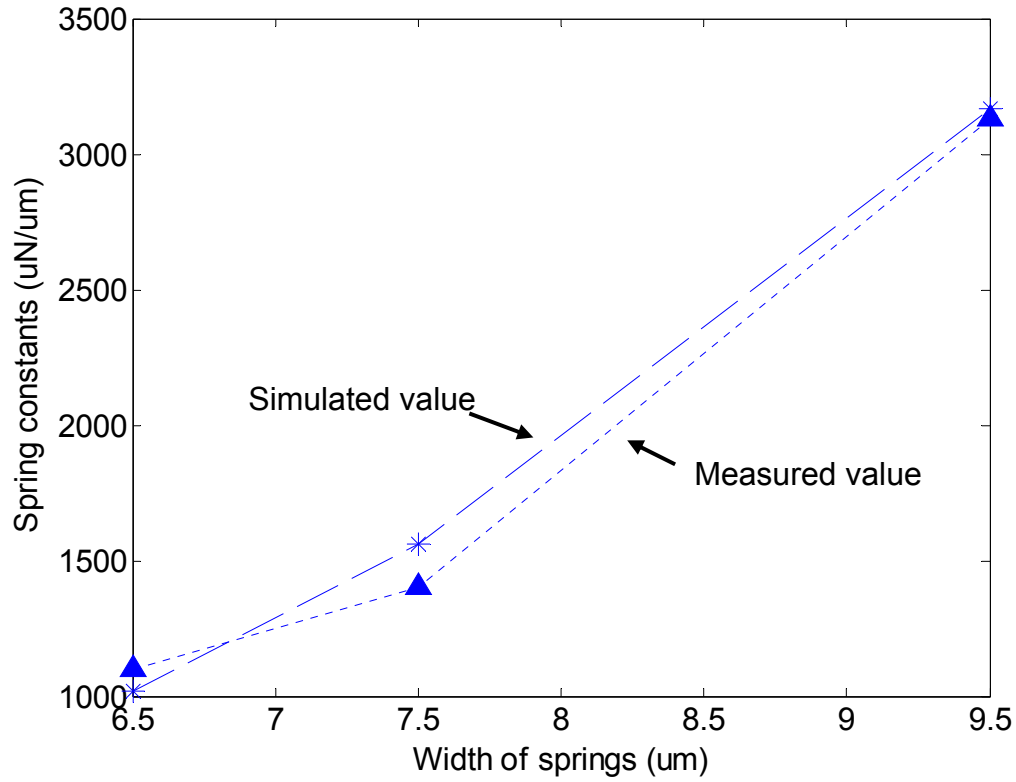


Figure 4.3 Measured and simulated spring constants with feature size shrinkage considered

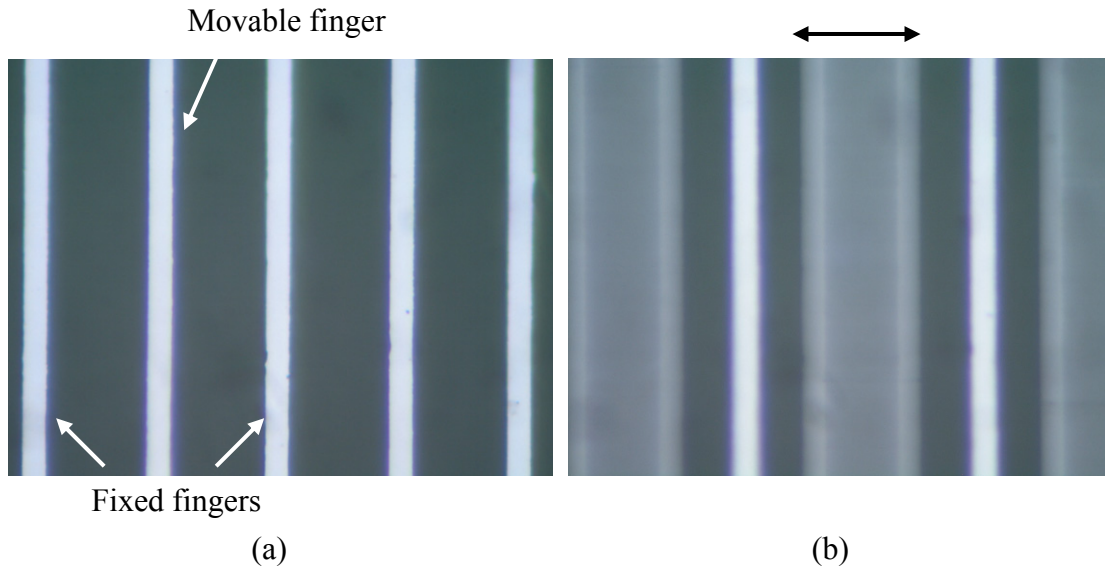


Figure 4.4 Fingers under (a) 0 Hz and (b) 2160Hz

The resonance of a device is shown in Figure 4.4. Figure 4.4 (a) shows comb fingers under static condition. In Figure 4.4 (b), the image of movable fingers becomes blurred at the resonant frequency of 2160 Hz.

MEMS Motion Analyzer (MMA) at the Chip Implementation Center (CIC) was also used to measure the dynamic response of the device. The pictures captured by the optical microscope were analyzed by image processing. As shown in Figure 4.5, the relative displacement  $Z$  is the displacement of the movable parts with respect to the fixed parts. Whereas the relative displacement  $Z$  represents the output, the input is represented by the vibration displacement of the fixed parts  $Y$ . The maximum displacement  $Z$  is about  $13.7 \mu\text{m}$  at 2160 Hz with the input vibration of  $0.27 \mu\text{m}$ . The corresponding acceleration calculated from the equation  $a=\omega^2Y$  is about  $50 \text{ m/s}^2$ , close to measured value of  $45 \text{ m/s}^2$  from the accelerometer.

The ratio of the output to the input  $|Z/Y|$  is also plotted in Figure 4.6 to show the system response. A second order model is used to fit the measured data by adjusting its resonant frequency, damping ratio and DC gain. The resulting quality



factor  $Q = \omega_0 / \Delta\omega$  is about 48, where  $\omega_0 = 2152$  Hz is the resonant frequency and  $\Delta\omega = 45$  Hz is the resonance bandwidth.

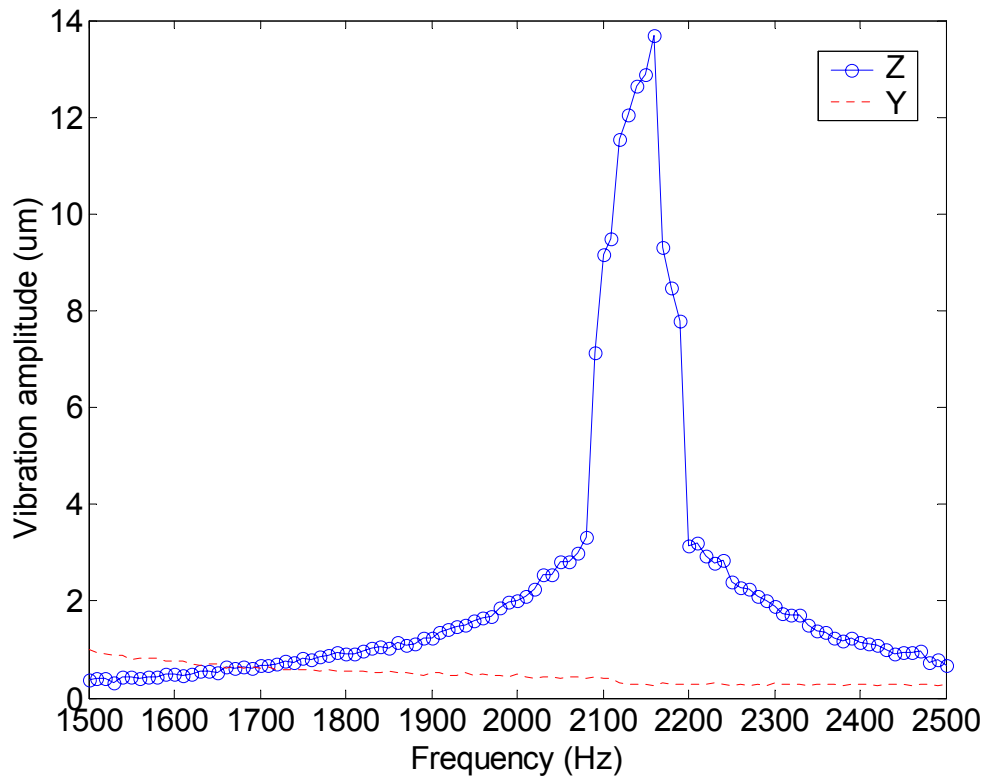


Figure 4.5 Displacement of Y and Z

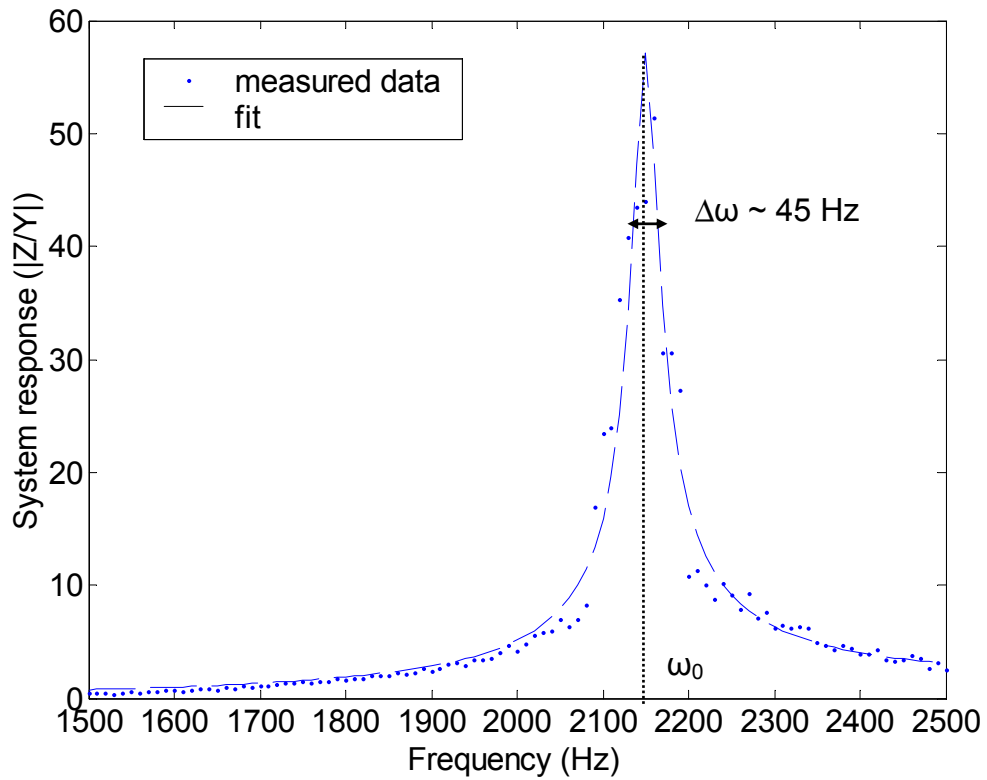


Figure 4.6 System response

If a steel ball (radius of 4 mm) of 2.1 gram was attached to a device with spring constant of  $3170 \mu\text{N}/\mu\text{m}$ , the resonant frequency was shifted to 156 Hz from 2160 Hz. However, the calculated resonant frequency with mass of 2.1 gram and spring constant of  $3170 \mu\text{N}/\mu\text{m}$  is about 185 Hz. The reason for this variation is still under investigation. As the applied acceleration became larger, the displacement also increased, as shown in Figure 4.7. Finally, at the acceleration of about  $16 \text{ m/s}^2$ , the displacement reached its maximum and the center plate started to collide with the mechanical stops. Unfortunately, the springs on one side broke when the collision lasted for too long.

According to the discussion in Chapter 2, the device was designed to reach its maximum displacement at  $2.25 \text{ m/s}^2$  acceleration with a 3.3 V applied DC voltage. The measured results showed that a larger acceleration ( $16 \text{ m/s}^2$ ) was needed without the 3.3 V DC voltage. As discussed in Chapter 2, the electrostatic force is proportional to the negative displacement of the movable plate. Therefore, it acts like a negative spring and decreases the total spring constant. Since the voltage was not applied, the total spring constant was larger than that with the applied voltage, it therefore explains why a larger acceleration was needed to reach the maximum displacement. The Simulink model was also used to simulate this situation. The result showed that an acceleration of about  $20 \text{ m/s}^2$  was needed to generate the maximum displacement.



Figure 4.7 Device resonance at 156 Hz with maximum displacement



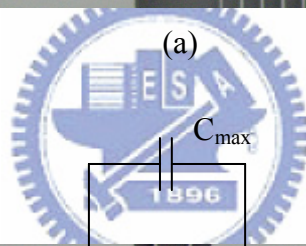
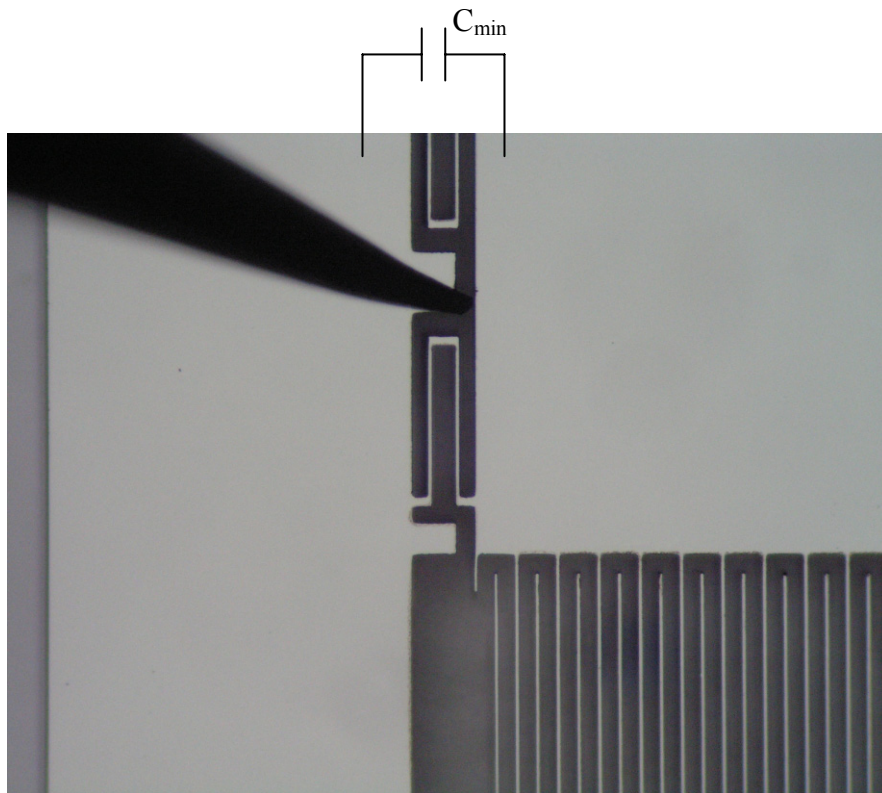
## 4.2 Electrical measurement

After the structure was released, the die was coated with aluminum of 5000 Å thickness. Without vibration, the impedance was measured using an INSTEK-LCR-816 LCR meter. The measured dummy parasitic capacitance of the probes was about 0.5 pF.

The variable capacitor at the minimum capacitance position is shown in Figure 4.8 (a). Without any displacement, the measured minimum capacitance was about 40~80 pF, varying from die to die. Since the calculated  $C_{\min}$  is about 44 pF, the measured parasitic capacitance of the device was less than 40 pF. Compared to the first generation devices which had a parasitic capacitance of more than 400 pF [27], the parasitic capacitance in the current devices has been greatly reduced due to the removal of the substrate below the center plate. With the large area removed, parasitic capacitance about 350 pF can be eliminated.

The resistance was also measured at the minimum capacitance position. The measured results showed the resistance was infinity, which meant no parallel conductance because all the shorted fingers were removed by the probes.

As shown in Figure 4.8 (b), the center plate was pushed to the maximum capacitance position by another probe that contributed negligible capacitance. However, due to the shrinkage of the finger width, the gaps between fingers could not be minimized when the center plate touched the mechanical stops. Hence, the measured maximum capacitance was only about 500~1000 pF, whereas the calculated  $C_{\max}$  at the minimum gap of 0.1 μm is about 6500 pF.



(b)

Figure 4.8 Variable capacitor at (a)  $C_{\min}$  position and (b)  $C_{\max}$  position

After the device measurement was conducted, the measured parameters can be used to estimate the predicted output power. Inserting the measured spring constant  $k$  of  $3170 \mu\text{N}/\mu\text{m}$  (with the corresponding attached mass of 2.1 gram),  $C_{\text{min}}$  of 40 pF, and  $C_{\text{max}}$  of 1000 pF into the simulation model, the simulated output power is about  $4.3 \mu\text{W}$  for  $R_L$  of  $8 \text{ M}\Omega$  and  $C_{\text{stor}}$  of 20 nF.

### 4.3 Output power measurement

The output power from the fabricated variable capacitor should be tested based on Figure 2.19. However, the AC current measurement was not conducted. The reason is that the devices were very fragile to shocks. First, one working device died during wire bonding process. Then, another device with the attached mass were broken during mechanical measurement. As a result, only one die was still alive but with many particles causing shortage. Due to the bad electrical properties of this die, the further electrical measurement was not performed. A new run for the device fabrication is in progress.

### 4.4 Conclusion

The measurement results were presented in this chapter. Device displacements and resonance were analyzed by MMA. Without the attached mass, the resonant frequency of 2160 Hz and quality factor of 48 were obtained. After an external mass was attached, the resonant frequency was shifted to 156 Hz. In the electrical measurement, the parasitic conductance was greatly reduced by removing the substrate below the center plate. The minimum capacitance ranged from 40 to 80 pF and the maximum capacitance was less than 1000 pF because of the shrinkage of the

finger width. Finally, a new run of fabrication is in progress for more devices for output power measurement.



## Chapter 5 Conclusions

### 5.1 Summary

In this thesis, the analysis and design of a micro vibration-to-electricity converter were accomplished. For the 3.3 V supply voltage and 1cm<sup>2</sup> chip area constraints, optimal design parameters were found from theoretical calculation and Simulink simulation. In the current design, the output power is 200  $\mu$ W for the optimal load of 8 M $\Omega$ .

The device was fabricated in a SOI wafer. The problems arising from fabrication were presented. Explanations for these problems as well as proposed solutions were also discussed.

The variable capacitor was vibrated on the shaker and displacements were recorded. The resonant frequency of the device without mass attachment was about 2160 Hz with a Q-factor of 48. With an attached mass, the resonant frequency was shifted to 156 Hz. Electrical measurements showed that the unwanted parasitic conductance was eliminated by backside etching. And the measured minimum and maximum variable capacitance are 40~80 pF and 500~1000 pF, respectively. AC current and output power measurement using schematic Figure 2.19 were not performed because no die with fine electrical properties survived.

Fabrication and measurement experiences were gained through the experiments. A new run for device fabrication and further device tests are being conducted. Improvement of the design and fabrication processes is suggested in next section.



## 5.2 Future work

First, improvements on the device fabrication should be noticed. In the current fabrication process, which is an expensive one, two DRIE steps and a SOI wafer are needed. Overall, this process is unnecessary to some extent. While SOI wafers are chosen to achieve electrical isolation and structure support, backside DRIE is used to remove partial SOI handle layer and eliminate parasitic capacitance. A new process utilizing a quartz wafer and only one DRIE step is introduced as shown in Figure 5.1. In a quartz wafer, pits are etched by HF solution to allow the moving mass to glide above them. A prime wafer is then bonded to the quartz wafer by an anodic bond. Once the wafers are securely bonded, the structure is defined by DRIE. Eventually, the quartz wafer contributes to no parasitic capacitance and provides electrical isolation and structure support.

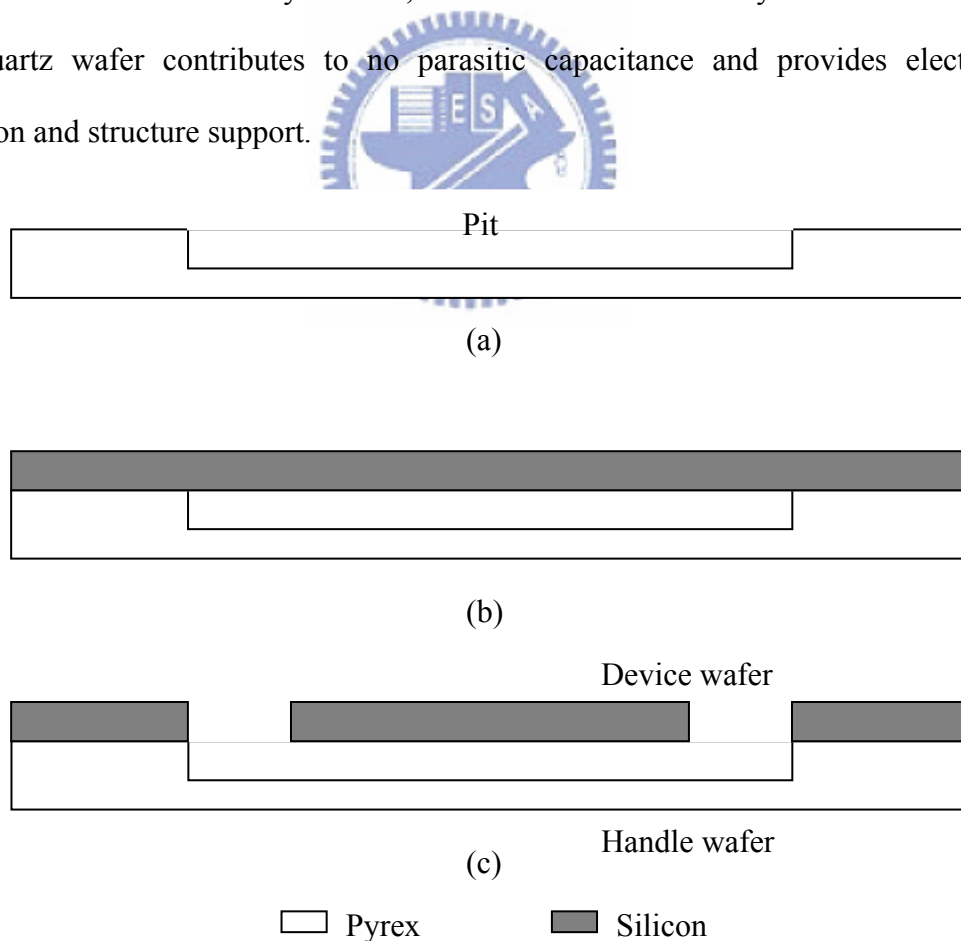


Figure 5.1 Improved device fabrication: (a) pit holes etched in a Pyrex wafer, (b) anodic bond and (c) structure defined by DRIE

Second, the energy conversion process needs an external DC voltage source such as a battery. This limits the applications of the converter. Advanced method using pre-charged electret as the initialize polarizing voltage source has been reported [38]. As shown in Figure 5.2, the variable capacitor is polarized by an electret. The variation of the capacitance results in a current through a load circuit. With the electret included, there will be no need of external battery and thus extend the application potential.

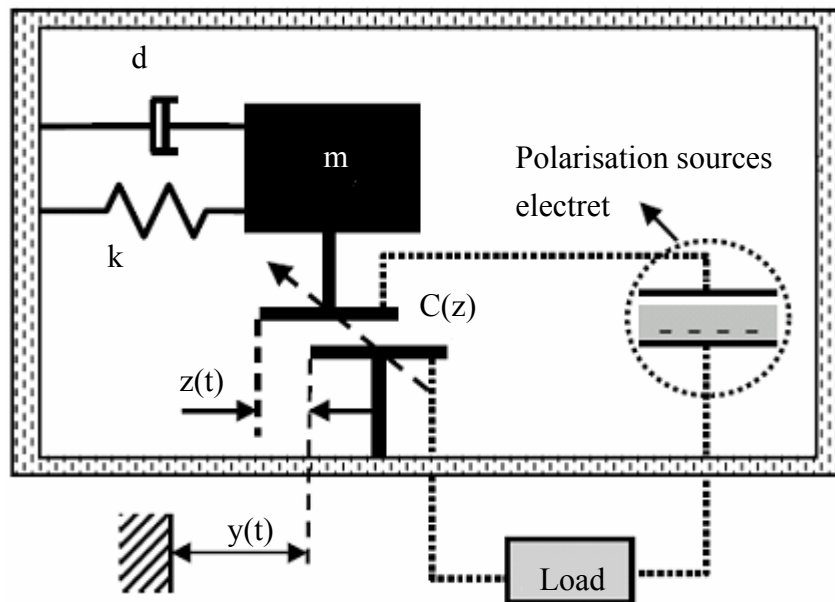


Figure 5.2 Principle of electret-based generator [38]

Regarding the fabrication processes, since the feature size shrinkage during device fabrication always exists, the compensation for the reduced variable capacitance should be done. Generally, the shrinkage of spring width reduces the spring constant and thus larger displacement of the device can be achieved. In other words, the increased minimum finger spacing (due to finger width shrinkage) and the reduced maximum capacitance are compensated. In the future, a more flexible design that tolerate wider range of reduced springs constants can be designed.

Finally, more efforts should be made on the device robustness. When the devices are subject to large acceleration, they are often broken because the center plate collides the mechanical stops. If the current minimum gap ( $0.1 \mu\text{m}$ ) controlled by the mechanical stops can be reduced to  $0 \mu\text{m}$ , the movable fingers will touch the fixed fingers each time the center plate collides the mechanical stops. The soft, insulated fingers act like a buffer that prevent the direct collision and thus enhance the device robustness. However, the stability of the device is still an issue when the bumps occur.



## Reference

- [1] B. Linden and T. Reddy, *Handbook of Batteries*, New York: McGraw-Hill, 2002.
- [2] J. Harb, R. LaFollette, R. Selfridge, and L. Howell, "Microbatteries for Self-sustained Hybrid Micropower Supplies," *Journal of Power Sources*, vol. 104, no. 1, pp. 46-51, 2002.
- [3] A. Heinzl, C. Hebling, M. Muller, M. Zedda, and C. Muller, "Fuel Cells for Low Power Applications," *Journal of Power Sources*, vol. 105, no. 2, pp. 250-255, 2002.
- [4] [www.nec-tokin.net/now/english/product/hypercapacitor/outline02.html](http://www.nec-tokin.net/now/english/product/hypercapacitor/outline02.html), 2003.
- [5] C. Lee, S. Arslan, Y. Liu, and L. Frechette, "Design of a Microfabricated Rankine Cycle Steam Turbine for Power Generation," *Proceedings of IMECE '03, ASME International Mechanical Engineering Congress & Exposition*, pp. 16-21, 2003.
- [6] H. Li and A. Lal, "Self-reciprocating Radio-isotope Powered Cantilever," *Journal of Applied Physics*, vol. 92, no. 2, pp. 1122-1127, 2002.
- [7] R. Russ, "Battery Power Trade-offs, Low Voltage or Higher Capacity?," *EE Times*, July, 2002.
- [8] A. Chandrakasan and R. Amirtharajah, "Self-powered Signal Processing Using Vibration-based Power Generation," *IEEE Journal of Solid-State Circuits*, vol. 33, no. 5, pp. 687-695, 1998.
- [9] S. Roundy, P. Wright, and J. Rabaey, *Energy Scavenging for Wireless Sensor Networks with Special Focus on Vibrations*, Kluwer Academic Press, 2003.
- [10] S. Kasap, *Optoelectronics and Photonics: Principles and Practices*, Prentice-Hall, 2001.
- [11] S. Lee, "Development of High-efficiency Silicon Solar Cells for Commercialization," *Journal of Korean Physical Society*, vol. 39, no.2, pp.

369-373, 2001.

- [12] E. Castano, E. Revuelto, M. Martin, A. Garcia-Alonso, and F. Garcia, "Metallic Thin-film Thermoelectric Microgenerator," *Sensors and Actuators A*, vol. 60, no. 1-3, pp. 65-67, 1997.
- [13] M. Stordeur and I. Stark, "Low Power Thermoelectric Generator-self-sufficient Energy Supply for Micro Systems," *Proceedings of XVI ICT '97, 16th International Conference on Thermoelectrics*, pp. 575-577, 1997.
- [14] S. Roundy, D. Steingart, L. Frechette, P. Wright, and J. Rabaey, "Power sources for Wireless Sensor Networks," *Proceedings of EWSN 2004, Wireless Sensor Networks, First European Workshop*, pp. 1-17, 2004.
- [15] N. Shenck and J. Paradiso, "Energy Scavenging with Shoe-mounted Piezoelectrics," *IEEE Micro*, vol. 21, no. 3, pp. 30-42, 2001.
- [16] T. Starner, "Human-powered Wearable Computing," *IBM Systems Journal*, vol. 35, no. 3-4, pp. 618-629, 1996.
- [17] J. Rabaey, M. Ammer, J. Silva, Jr, D. Patel, and S. Roundy, "PicoRadio Supports Ad Hoc Ultra-low Power Wireless Networking," *IEEE Computer*, vol. 33, no. 7, pp. 42-48, 2000.
- [18] E. Torres and G. Rincón-Mora, "Long-Lasting, Self-Sustaining, and Energy-Harvesting System-in-Package (SiP) Wireless Micro-Sensor Solution," *Proceedings of International Conference on Energy, Environment and Disasters (INCEED 2005)*, pp. 1-33, 2005.
- [19] C. Williams and R. Yates, "Analysis of a Micro-electric Generator for Microsystems," *Sensor and Actuators A*, vol. 52, no. 1-3, pp. 8-11, 1996.
- [20] C. Shearwood and R. Yates, "Development of an Electromagnetic Microgenerator," *Electronics Letters*, vol. 33 pp. 1883-1884, 1997.
- [21] A. Chandrakasan and R. Amirtharajah, "Self-powered Signal Processing Using

- Vibration-based Power Generation,” *IEEE Journal of Solid-State Circuits*, vol. 33, no. 5, pp. 687-695, 1998.
- [22] S. Meninger, J. Mur-Miranda., R. Amirtharajah, A. Chandrakasan, and J. Lang, “Vibration-to-electric Conversion,” *Proceedings of 1999 International Symposium on Low Power Electronics and Design*, pp. 48–53, 1999.
- [23] S. Meninger, J. Mur-Miranda., R. Amirtharajah, A. Chandrakasan, and J. Lang, “Vibration-to-electric Conversion,” *IEEE Transactions on Very Large Scale Integration Systems*, vol. 9, no. 1, pp. 64-76, 2001.
- [24] S. Roundy, E.S. Leland, J. Baker, E. Carleton, and E. Reilly, “Improving Power Output for Vibration-based Energy Scavengers,” *IEEE Pervasive Computing*, vol. 4, no. 1, pp. 28-36, 2005.
- [25] G. Ottman, H. Hofmann, and G. Lesieutre, “Optimized Piezoelectric Energy Harvesting Circuit using Step-down Converter in Discontinuous Conduction Mode,” *IEEE Transactions on Power Electronics*, vol. 18, no. 2, pp. 696-703, 2003.
- [26] G. Ottman, H. Hofmann, A. Bhatt, and G. Lesieutre, “Adaptive Piezoelectric Energy Harvesting Circuit for Wireless Remote Power Supply,” *IEEE Transactions on Power Electronics*, vol. 17, no. 5, pp. 669-76, 2002.
- [27] Y. Chu, “A MEMS Electrostatic Vibration-to-electricity Energy Converter,” *Proceedings of PowerMEMS 2005*, pp. 49-52, 2005.
- [28] J. Starr, “Squeeze-film Damping In Solid-state Accelerometers,” *IEEE Solid-State Sensor and Actuator Workshop. Digest of Technical Papers*, pp. 44-47, 1990.
- [29] M. Andres, I. Harris, and G. Turner, “A Comparison of Squeeze-film Theory with Measurements on a Microstructure,” *Sensor and Actuators A*, vol. 36, no. 1, pp. 79-87, 1993.

- [30] S. Roundy, P. Wright, and K. Pister, "Micro-electrostatic vibration-to-electricity Converters," *Proceedings of IMECE '02, ASME International Mechanical Engineering Congress & Exposition*, pp. 17-22, 2002.
- [31] R. Legtenberg, A.W. Groeneveld, and M Elwenspoek, "Comb-drive Actuators for Large Displacements," *Journal of Micromechanics & Microengineering*, vol. 6 no. 3, pp. 320-329, 1996.
- [32] M. Judy, "Micromechanisms Using Sidewall Beams," *Ph.D thesis, Department of Electrical Engineering and Computer Sciences, University of California, Berkeley*, 1994.
- [33] J. Bates, N. Dudney, B. Neudecker, A. Ueda, and C. Evans, "Thin-film Lithium and Lithium-ion Batteries," *Solid State Ionics, Diffusion & Reactions*, vol. 135, no. 1-4, pp. 33-45, 2000.
- [34] J. Mur-Miranda, "Electrostatic Vibration-to-electric energy conversion," *Ph.D thesis, Department of Electrical Engineering and Computer Sciences, Massachusetts Institute of Technology*, 2004.
- [35] W. Chu, M. Mehregany, D. Hansford, and P. Pirouz, "Effect of Thermal Oxidation on Residual Stress Distribution through the Thickness of p+ Silicon Films," *IEEE Solid-State Sensor and Actuator Workshop. Digest of Technical Papers*, pp. 90-93, 1992.
- [36] Y. Sun, D. Piyabongkarn, A. Sezen, B.J. Nelson, and R. Rajamani, "A High-aspect-ratio Two-axis Electrostatic Microactuator with Extended Travel Range," *Sensor and Actuators A*, vol. 102, no. 1-2, pp. 49-60, 2002.
- [37] N. Belov and D. N. Khe, "Using Deep RIE for Micromachining SOI Wafers," *Proceedings of 52nd IEEE Electronic Components and Technology Conference*, pp. 1163-1166, 2002.
- [38] T. Sterken, P Fiorini, K Baert, R. Puers, and G. Borghs, "An Electret-based

Electrostatic  $\mu$ -Generator,” *Transducers '03, 12th International Conference on Solid-State Sensors, Actuators and Microsystems. Digest of Technical Papers*, vol. 2, pp. 1291-1294, 2003.

